Healthcare Monitoring of Bone Fracture Healing by Implanted Antenna

Wael A. Zeinelabedeen Elwaseef

Submitted to the
Institute of Graduate Studies and Research
in partial fulfillment of the requirements for the degree of

Doctor of Philosophy
in
Electrical and Electronic Engineering

Eastern Mediterranean University
February 2022
Gazimağusa, North Cyprus

Approval of the Institute of Graduate Studies and Research

Prof. Dr. Ali Hakan Ulusoy
Director

I certify that this thesis satisfies all the requirements as a thesis for the degree of Doctor of Philosophy in Electrical and Electronic Engineering.

Assoc. Prof. Dr. Rasime Uyguroglu
Chair, Department of Electrical and Electronic Engineering

We certify that we have read this thesis and that in our opinion it is fully adequate in scope and quality as a thesis for the degree of Doctor of Philosophy in Electrical and Electronic Engineering.

Assoc. Prof. Dr. Rasime Uyguroglu
Supervisor

Examining Committee

1. Prof. Dr. Mustafa Kuzuoglu

2. Prof. Dr. Abdullah Y. Oztoprak

3. Prof. Dr. Birsen Saka Tanatar

4. Prof. Dr. Sener Uysal

5. Assoc. Prof. Dr. Rasime Uyguroglu

ABSTRACT

Remote patient monitoring using implantable medical devices (IMDs) provides continuous health monitoring such as heart rate, blood pressure, or insulin level through telecommunications. Wireless biotelemetry allows the transmission of physiological signals from the implanted device to monitoring or controlling devices. This thesis is about the study and characterization of the inhomogeneous human tissue as the lossy part of the communication channel. A healthcare monitoring technique of bone fracture healing is proposed. A multilayer human tissue model is analyzed in a range of frequencies covering the MICS and ISM bands for this purpose. The range of in-to-out incident angle of electromagnetic wave which produces transmission outside the body is identified for each frequency. The variation of reflection coefficient at the borders of the tissues with incident angle is characterized. An additional layer is added to the multilayer model to represent the fracture which increases the loss inside the model and affects the transmitted average power density outside the body. The human femoral shaft fractures and humerus fractures are selected as the applications of the proposed monitoring technique. Two post-surgery treated models of femoral shaft and humerus fractures are simulated by CST Microwave studio using different topologies of linear and meander half wave dipole antennas. The technique is verified experimentally on lifeless animal models and the measurements show good matching with the simulation results. This monitoring technique avoids repeated exposing to X-Ray and eases the patients' life through monitoring at home.

Keywords: implanted antenna, oblique incidence, monitoring, fracture healing

ÖZ

Vücuda yerleştirilebilir tıbbi cihazlar (IMD'ler) kullanılarak uzaktan hasta izleme, telekomünikasyon yoluyla kalp hızı, kan basıncı veya insülin seviyesi gibi sürekli sağlık izlemesi sağlar. Kablosuz biyotelemetri, fizyolojik sinyallerin implante edilmiş cihazdan izleme veya kontrol cihazlarına iletilmesine izin verir. Bu tez homojen olmayan insan dokusunu iletişim kanalının kayıplı kısmı olarak incelemiş ve karakterize etmiştir. Çok katmanlı bir insan doku modeli önerilmiş ve MICS ve ISM bantlarını kapsayan bir dizi frekansta analiz edilmiştir. Her frekans için, vücut dışında iletim oluşturan elektromanyetik dalganın içeri-dışa geliş açısı aralığı belirlenir. Dokuların sınırlarındaki yansıma katsayısının geliş açısı ile değişimi karakterize edilir. Kemik kırığı iyileşmesinin sağlık bakımında izlenmesi önerilmektedir. Model içindeki kaybı artıran ve gövde dışında iletilen ortalama güç yoğunluğunu etkileyen kırılmayı temsil etmek için modele ek katman eklenir. Önerilen izleme tekniğinin uygulamaları olarak insan femur cisim kırıkları ve humerus kırıkları seçilmiştir. Femur şaftı ve humerus kırıklarının ameliyat sonrası tedavi edilen iki modeli, farklı lineer ve menderes yarım dalga dipol antenleri kullanılarak CST Microwave stüdyosu tarafından simüle edilmiştir. Teknik, cansız hayvan modellerinde deneysel olarak doğrulanmıştır ve ölçümler simülasyon sonuçlarıyla iyi bir uyum göstermektedir. Bu izleme tekniği, X-Ray'e tekrar tekrar maruz kalmayı önler ve evde izleme yoluyla hastaların hayatını kolaylaştırır.

Anahtar Kelimeler: implante edilmiş anten, eğik insidans, izleme, kırık iyileşmesi

DEDICATION

To my lovely wife Lamia

To Abdullah, Maryam, Menna, Omar and Malek

ACKNOWLEDGMENT

First and foremost I am extremely grateful to my supervisor Assoc. Prof. Dr. Rasime Uyguroglu for her invaluable advice, continuous support, and patience during my PhD study. Her immense knowledge and plentiful experience have encouraged me in all the time of my academic research and daily life. I would also like to thank prof. Dr. Sener Uysal and Prof. Dr. Abdullah Oztoprak for their guiding and support on my study. Finally, I would like to express my gratitude to my wife, my sons and daughters. Without their tremendous understanding and encouragement in the past few years, it would be impossible for me to complete my study.

TABLE OF CONTENTS

LIST OF TABLES

LIST OF FIGURES

LIST OF SYMBOLS AND ABREVIATIONS

D	Electric flux density
D_m	Antenna dimension
E	Electric field intensity
H	Magnetic field intensity
$l_{rad_{max}}$	Maximum radiation length
P_{abs}	Absorbed power
P_i	Dissipated power in layer i
$P_{l_{max}}$	Maximum propagation path length
P_{rad}	Radiated power
P_{source}	Source power
Re	Real
R_l	Load resistance
R_{rad}	Radiation resistance
S_{av}	Time average pointing vector
T	Transmission coefficient
X_A	Reactance
Z_A	Antenna impedance
Σ	Conductivity
ε_o	Free space permittivity
ε_r	Relative permittivity
ρ	Charge density
γ	Propagation constant
ω	Angular frequency

μ_0	Free space permeability
μ_r	Relative permeability
Γ	Reflection coefficient
β	Phase constant
θ_i	Incident angle
θ_t	Transmission angle
θ_{obs}	Observation angle
α	Attenuation constant
λ	Wavelength
AMPD	Average monitoring power density
CT	Computed tomography
EM	Electromagnetic
ERCC	European radio communications commissions
FCC	Federal communications commissions
IMD	Implantable medical device
ISM	Industrial, scientific and medical
MICS	Medical implant communication service
MRI	Magnetic resonance imaging
PCB	Printed circuit board
PIFA	Planar inverted F antenna
RFID	Radio frequency identification
RPM	Remote patient monitoring
SAR	Specific absorption rate
SMA	Sub-miniature version A
UWB	Ultra-wide band

WBAN	Wireless body area network

Chapter 1

INTRODUCTION

1.1 Overview

Conventional technologies such as mammography and computed tomography (CT scan) which is described by Cormack in 1963 using the X-ray discovered by Rontgen in 1895, sonography using ultrasound, magnetic resonance imaging (MRI) using magnetic fields that is tested firstly in 1980, are widely used for medical diagnosis (such as cancer, bone imaging, etc.). These technologies provide good sensitivity regarding the image contrast between the different tissues and good spatial resolution in the sub-millimeter range. However, these technologies have its draw backs [1].

The MRI system is not willingly available at all hospitals due to the bulky machinery required, the high manufacturing cost and the relatively long scan and post processing time. Mammography and CT scan, using ionizing radiation, are techniques with intrinsic hazards and increase the risk of cancer incidence. Moreover, the painful examinations associated with mammography have to be tolerated by the patients. The ultrasound technique examines without ionization and is preferred for medical diagnosis. However, it cannot penetrate bones and air due to their strong reflections that cause acoustic shadows.

In contrast with the risks and disadvantages associated with these technologies, the microwave technique for medical applications uses non-ionizing electromagnetic

waves, which makes it less harmful for the patients compared to mammography and CT scan. Microwaves at low frequencies (below 2GHz) feature good penetration ability into all human tissues including the bones, in which ultrasound has difficulty to penetrate. A high resolution for microwave medical imaging can be achieved by using wideband microwave signals. Furthermore, microwaves within the same frequency range allow a combination of diagnosis and wireless data transmission, which is not possible using any other technologies for medical applications.

1.2 Microwave medical applications

Currently, the microwave applications in medical field are in healthcare monitoring, medical diagnosis and treatment.

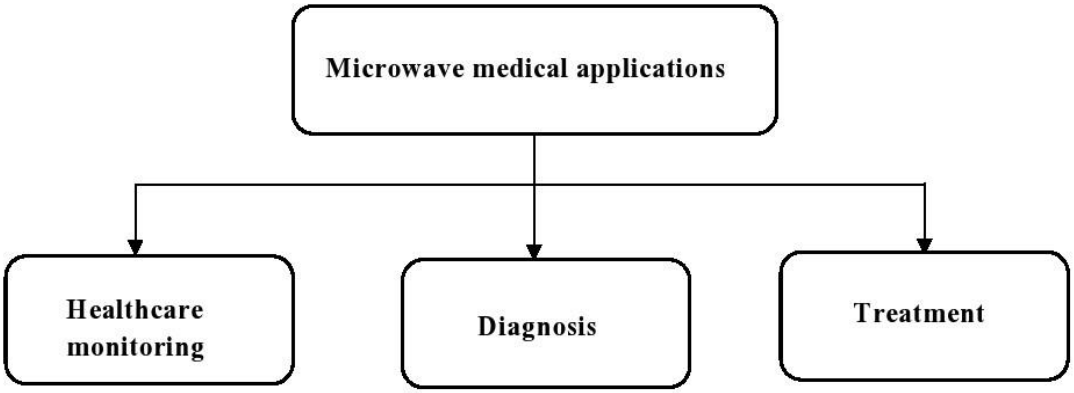

Figure 1. Microwave medical applications.

In healthcare monitoring or data telemetry, the wireless data is transmitted between the wearable or implanted medical device to an external device for monitoring the physiological status of the patient. Potential applications of the data telemetry are such as in glucose monitoring for diabetics, cochlear implants, and deep brain stimulation. For glucose monitoring for diabetics, the glucose level is recorded by an implanted biosensor and transmitted by an implantable antenna to the external devices. In the

application of cochlear implants, the audio signal can be transmitted directly by an external antenna attached behind the ear to the receiver in the cochlea (cochlear implant). Other applications using data telemetry such as wireless monitoring of body temperature, blood pressure and heart beat rate are addressed in the literature.

The applications for medical diagnosis are in the detection of stroke, water accumulation in human body, and one of the most important applications of medical diagnosis is the detection of breast cancer, which is the most prevalent form of cancer among women [2].

Microwave medical diagnosis is based on the concept of observing the reflected signals caused by the dielectric contrast, which is the difference of the dielectric properties between the diseased tissues and the surrounding healthy tissues [3].

Medical treatment using microwaves is based on using the heat generated by microwave radiation to increase the local temperature to destroy the abnormal tissues (e.g. malignant tissues). This heat is a result of electromagnetic (EM) field absorbed by the human tissue. The amount of absorption and heat conversion depends on the electrical properties of the tissue. This technique is more sensitive and effective compared to ionizing radiation as X-ray and chemical toxins like Chemotherapy [4].

1.3 Remote patient monitoring

Remote patient monitoring is a method of healthcare delivery that uses the state-of-the-art advances in information technology to gather patient data outside of traditional healthcare settings. The advances in telecommunication technology, miniaturization of implantable and wearable medical devises open a creative and cost effective solutions for delivering healthcare remotely.

Recently, the need to adopt advanced health technology has increased as covid-19 spreads rapidly across the world and global healthcare infrastructure become overloaded with covid-19 cases, the applications of remote patient monitoring are becoming more important.

Remote healthcare monitoring targets several subcategories of patients such as patients diagnosed with chronic disorders, patients with movement issues, or other disability, and post-surgery patients. These patients have conditions that are better to be monitored continuously. The goal of the remote healthcare monitoring is to support ordinary life as much comfort as possible to all patients [5].

Common models of remote health monitoring devices include continuous glucose monitoring that remind diabetes patients to take their insulin, while allowing their physician to monitor the disease, digital blood pressure monitoring that enable patients to remotely send physicians their blood pressure and blood oxygen levels.

Biomedical devices are classified into on-body or wearable devices and in-body or implantable devices according to their location. The choice depends on the application, economic aspects, and the technological challenges [6].

The wearable devices exist in our life as in smart watch and wristbands with sensing capability. In the healthcare system, the on-body devices enable monitoring of noninvasive vital signs. However, certain challenges remain unsolved, among them, miniaturization, security, standardization, energy efficiency, robustness and unobtrusiveness.

Most of the in-body devices are still in development and require a specific medical prescription to be used. The first appearance of implanted devices was in 1958 when *Rune Elmgvist* succeeded in implanting the first pacemaker in human body [7]. These devices cover the area when the physiological parameters are only accessible from inside the body or when the wearable devices are not sufficiently powerful. Apart from the pacemakers and some ingestible endoscopic capsules with biotelemetry capability, most of the in-body devices are still in development or testing or in prototyping stage. The list of challenges to be overcome is longer and more demanding than in the wearable devices such as a greater level of miniaturization, biocompatibility and safety considerations.

Several technologies have been proposed as possible solutions for both in-body and on-body devices' challenges. Among them is the RFID technology which provides low power and low cost devices. The RFID system provides standardized communication protocol and integrated commercial chips which facilitate the development of medical devices with wireless biotelemetry. The RFID systems are expanding from the industrial to the healthcare sector especially for the identification and tracking of the patients [8].

With the fast development of biomedical engineering, implantable medical devices (IMD) are promising to be widely used in medical diagnosis, treatment and health care monitoring applications such as pacemakers, heart rate, and blood pressure monitoring [9]-[13]. The operation of these applications needs to set up a connection between the implanted device within the human body and the outside base station or controlling device. The physiological signal, which is an EM wave, propagates from the implanted device through a multilayer human tissue before elaborating out of the body to the

external device. The signals are retransmitted through the internet to the hospital or clinical laboratory for monitoring [14].

As the human body is a lossy medium which considerably attenuates the travelling EM wave [15]-[17], accurate knowledge and investigation of the EM properties of biological tissues and characteristic behaviour of the body channel are the key roles to set up the communication. Conductivity and permittivity characteristics describe the EM wave properties such as attenuation, propagation velocity and wavelength in the human tissue propagation medium.

Figure 2 shows the basic elements of remote patient monitoring (RPM). The implanted device within the human body contains an antenna to transmit the collected data physiological signal as EM wave through the communication channel to the base station outside the body.

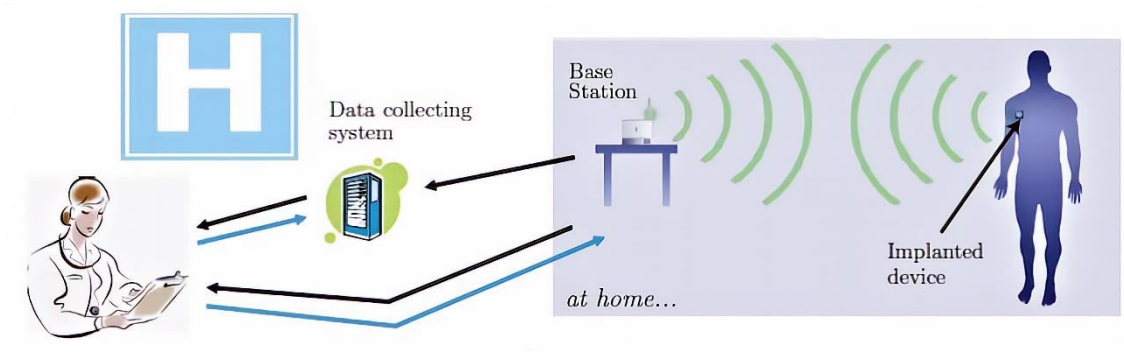

Figure 2. Remote patient monitoring system.

The choice of the antenna type and shape of radiator plays a key role in providing the wireless capability of the medical implanted device. The main quality criterion in the design is the amount of power transmitted by the antenna out of the body [18]-[21]. Implanted biomedical devices have become very essential in a large range of medical

applications such as: intracranial pressure monitoring, continuous blood pressure measurements, glucose monitoring, and bladder pressure monitoring, and controlling heartbeat [13],[22]-[24].

The goal of the antenna designer is to provide suitable design in terms of operating frequency, efficiency, radiation pattern taking in consideration the available volume, the interaction between the propagating EM wave and the human body and the influence of the other electronic components on the antenna efficiency.

The base station includes a receiver system, control module to drive the entire system and to store the measurements, and internet modem to connect to the data collecting system at the hospital or clinical laboratory.

The analysis of the EM propagation is an important aspect as part of the communication channel is the human body which is a lossy media. Multipath propagation and scattering due to the nearby objects, multiple reflection due to the biological composition of human tissue must be considered to improve the overall performance of the system.

The biocompatible insulation is mandatory for the implanted device to avoid any adverse reaction from the human tissue or rejection of the implant.

The electronic components allow the functioning of the implanted device. It is powered up internally by power supply which may occupy a large volume, or by wireless power transfer.

1.4 Frequency bands

The Federal Communications Commissions FCC and European Radio communications Commissions ERCC approved two frequency bands for implanted and wearable antennas. The ultra-wide band UWB applications (3.1-10 GHz) and the narrow band NB applications which include the medical implant communication system MICS (402-405 MHz) and the industrial, scientific and medical ISM band (2.45-2.5 GHz).

The European standardization technical institute standardized the MICS band. This standard lists two fields of applications. The first one is for the communication between the implants and the base station while the second one set the rules of telecommunications between the medical implants within the same body.

The bandwidth of the MICS band is limited to 300 KHz. To get a high data rate, a half-duplex scheme can be implemented. In this case, the system can use two frequencies for up and down link where one device can transmit at time. In case of full duplex scheme, the transmitting and receiving bandwidths must not add up to more than 300 KHz.

The ISM band is used by many services such as Wi-Fi, Bluetooth, microwave oven, etc. This is a disadvantage of the ISM band that raise the requirement of security system. The penetration into human body is also less than the MICS band while the size of the implanted antenna is smaller than that in the MICS band.

1.5 Benefits of remote patient monitoring

From increasing access to virtual care, increased patient-provider communication opportunities, and improved patient involvement in self-management, there are many important benefits to consider [25] as:-

1.5.1 Develops data driven clinical decision making

Remote patient monitoring helps in continuous following up the patient status to see the nuances and changes that are happening in the moment and alter the care plan accordingly.

1.5.2 Cost reduction of healthcare care for payers and providers

Remote patient monitoring has demonstrated significant impact in reducing potentially avoidable Emergency departments (ED) utilization as well as a reduction in unnecessary hospital admissions and readmission. Movement of appropriate levels of acute care and chronic care monitoring into the home, reduces the high costs of inpatient services.

1.5.3 Optimize clinical staff efficiency and struggles shortage

Remote patient monitoring benefits clinicians by helping them prioritize care delivery, enabling them to triage each patient and case based on close to real-time patient status. In the case of staffing shortages, RPM can help reduce the burden of over-scheduled in person visits by allowing clinicians to provide some of that care virtually. It leverages a team-based care model that allows for provider flexibility.

1.5.4 Prevent the spread of infectious diseases

With RPM, patients do not have to visit the hospital or clinic where they are vulnerable to contract an infection. Avoiding an in-person visit eliminates the risk of unnecessary exposure particularly for the elderly and those who are chronically ill or pregnant, etc.

1.5.5 Improve access to care and build patient engagement

Remote patient monitoring bridges the barrier of access by providing care to patients where they are, when they need it. It can be used to reach patients in rural areas, and connect patients to specialists remotely. It provides the patient with tools to assist them in understanding their health situation. When patients understand their conditions, their unique care plan, and what their responsibility is in improving their health, they are more likely to experience positive health outcomes.

1.6 Challenges of remote patient monitoring

The challenges that must be taken into account to help in wide spread using of the remote healthcare monitoring system can be categorized into social and cultural challenges, related to the personal nature of the patient and technical challenges of wireless transmission of data between the wearable or implanted medical device and the monitoring or controlling device [26].

1.6.1 Societal and culture challenges

Beside the technological challenges that are faced by the remote patient monitoring, altering the patients' minds and convincing them to the advantages of this type of healthcare delivery is another challenge. Elders usually feel comfort in physical proximity to doctors, nurses, or laboratory physicians. Patients must be well educated and trained to access the information related the remote delivery of psychological data to hospitals and clinical laboratories. Health care providers need to be aware of the cost-effectiveness of the shift to this mode of remote patient monitoring solutions.

1.6.2 Power limits (consumption)

Power consumption is one of the significant challenges in RPM systems. Batteries are the main source of energy in WBANs. The frequent recharging the battery may burden the patients and replacing them needs surgical operation as in the case of heart

pacemaker devices. Improving the protocols used in WBAN like Bluetooth and Zigbee for reduced power is an area of research. Printed thin film batteries, specially designed low power radio chips for WBANs have been developed. Passive implant can be a solution for powering the IMD where the implanted device is powered wireless by the Reader or controlling device when the transmission is needed as in RFID systems. Another solutions like using of solar cells are also being investigated [26].

1.6.3 Antenna size

The volume of the implanted device including the antenna, electronics, battery, sensors, etc., must be fit in a housing that has an ergonomic shape. This miniaturization requires a dense packaging and well integration of all components. Since the antenna occupies most of the available volume, miniaturization techniques have to be taken into account in antenna design and manufacturing.

Early studies in antenna miniaturization show that reducing the size of the antenna results in a direct reduction in its efficiency and bandwidth. Many recent investigations have been carried out to reduce the overall size of different types of antennas while maintaining acceptable matching properties and bandwidth. These techniques are depending mainly on changing the physical and electrical properties of the antenna. The most significant miniaturization techniques are divided into two main categories, *first,* topology based techniques where the idea is to use the available space or volume efficiently to design a larger radiating structure, like meander and fractal antennas. *Second,* material based miniaturized techniques which is based on changing the electric and magnetic properties of the antenna structure [27].

1.6.4 Biocompatibility

Implantable antennas must be biocompatible to ensure patient safety and prevent implant rejection. Isolating the metallic radiator from the human tissue employing a

biocompatible substrate and insertion of thin layer of low loss biocompatible coating is a technique to preserve the biocompatibility of the antenna (Bio-compatible encapsulation) [28].

1.6.5 Composition and electrical properties of human tissues

The electrical permittivity and conductivity of the biological tissue define the interaction between it and the propagating electromagnetic wave. The lossy tissues present high attenuation rates of the EM waves. Furthermore, the reflected fields at the interfaces of the tissues and at the body air interface give rises to the complication of predicting the EM behavior of an antenna implanted within the body or in close proximity to it.

1.6.6 Security issues

As the internet is the main medium for data collecting and transmitting to the specialists in hospitals and clinics, this raises the need for privacy and security issues in accessing these data. Examples of the attacks that are likely to occur in the healthcare systems are eavesdropping, impersonation, and data modifications. The implanted devices designed for remote patient monitoring are small devices with limited data storage and data processing capability. From this point of view it is difficult to implement powerful security algorithms in them. New innovative researches are required to achieve an acceptable level of security.

1.7 Thesis contribution

This study proposes a new solution, by implanted antenna, for the monitoring of bone fracture healing. Femoral shaft and humerus fractured are considered for this monitoring application. The femur fracture should be healed within 3 months. The traditional monitoring is by repeated X-Ray images and visits to clinical laboratories or hospitals which is difficult especially for elder patients. Our goal is to avoid this difficulty and to ease the patient's life during the long treatment period. This fracture is treated surgically and the proposed monitoring technique is by implanting an

antenna at the boundary between the fractured shaft and the muscle tissue within the human body during the surgical operation. The difference between the transmitted average power density in cases of normal and fractured bone provides information about the healing status. To achieve our goal we introduce two different models for the human tissues and study characteristics of the EM wave propagation from in-to-out the body. In addition to the new monitoring method, to the limit of our knowledge this is the first time to study the range of incident angles that produce transmission of EM wave from in-to-out the human tissues and the studies on the oblique incidence of EM wave on human tissues are limited. We analyze and evaluate the characteristics of the medium and the range of incident angles in a range of frequencies from 100 MHz to 10 GHz by codes written in MATLAB and use the results to select the operating frequency. The monitoring technique is simulated by CST Microwave studio software for the most common types of fractures and show good results by planar and meander half wave dipole antennas. The specific absorption rate SAR is simulated and the excitation signal is selected to satisfy the SAR standard limits and to be sure that the implanted antennas are safe for human tissues. The measurement and verification are carried out on non-living animal model. The results of measurements show good agreement with the simulation.

1.8 Thesis organization.

Chapter 1. Introduction.

Chapter 1 is an introduction states the advantages of the microwave medical applications over the conventional technology. We discuss the remote patient monitoring and its challenges as a promising health care technology.

Chapter 2. EM wave incidence on multilayer lossy tissue.

Understanding and characterization of body channel communication in a frequency range from 100 MHz to 10 GHz are presented in this chapter. A study on the range of incident angles of EM wave on multilayer human tissue model is included to specify the range of incident angles that produce transmission outside the body to set up a valid in-to-out body communication.

Chapter 3. Antenna within human body.

This chapter discusses the general characteristic of implanted antennas within human body. The half wave dipole antenna operation in transmitting and receiving is introduced as the selected type of antenna for the proposed healthcare application. We study the effect of lossy tissue surrounding the antenna on its performance. Finally the advantages and disadvantages of this type of antennas are presented.

Chapter 4. Healthcare monitoring application.

In this chapter, the monitoring of bone fracture healing is proposed as a remote patient monitoring application. The fractures types in human femoral shaft and upper arm are discussed. The bone healing process which are common for all bone fractures are explained. The advantages of the proposed method over the traditional monitoring is also presented.

A multilayer tissue model is analyzed in the studied range of frequencies with respect to the reflection coefficient at the borders between the tissue layers, the average power density propagated along the model, and the transmitted average power density outside the body and the specific absorption rate. From this study, the operating frequency of the proposed application is selected.

Chapter 5. Simulation and measurements.

A design and simulation of the implanted antennas for monitoring fractures healing in human femoral shaft and upper arm are introduced. The validation of the proposed monitoring technique is carried out on non-living animal models. Comparison between the simulation and measurements results are illustrated.

Chapter 6. Conclusion.

This chapter present a summary of the whole work performed in the thesis in addition to suggested future work.

Chapter 2

EM WAVE INCIDENCE ON MULTILAYER LOSSY TISSUE

A simplified model of multilayer human tissues is composed of consecutive bone, muscle, fat, and skin. The model is used to observe the effect of incident angle of EM wave on the in-to-out interfaces with the output transmission angle outside the body. Two cases are considered, when the EM wave propagation is through bone, muscle, fat, skin, to air and when it is through muscle, fat skin, to air. The model is shown in Figure 3 [29].

2.1 Maxwell's equations

Maxwell's equations for isotropic non-magnetic lossy material with conductivity σ and permittivity ε_r in point form for time varying fields are [30]:

$$\nabla \times \bar{E} = -\mu_o \frac{\partial \bar{H}}{\partial t} \tag{2.1}$$

$$\nabla \times \bar{H} = \sigma \bar{E} + \varepsilon_o \varepsilon_r \frac{\partial \bar{E}}{\partial t} \tag{2.2}$$

$$\nabla . \bar{D} = \frac{\rho}{\varepsilon} \tag{2.3}$$

$$\nabla . \bar{H} = 0 \tag{2.4}$$

Where μ_o and ε_o are the free space permeability and permittivity and ε_r is the relative permittivity of the medium. If sinusoidal and planar waves are considered, with electric field oriented in x direction and magnetic field oriented in y direction, and after making some calculations, wave equations are obtained:

$$\frac{\partial^2 E_x}{\partial Z^2} = \gamma^2 E_x \tag{2.5}$$

$$\frac{\partial^2 H_y}{\partial Z^2} = \gamma^2 H_y \tag{2.6}$$

Where γ is the propagation constant of the wave.

The solution of the second order differential equations for the electric and magnetic fields gives:

$$E_x = E_+ e^{-\gamma z} + E_- e^{\gamma z} \tag{2.7}$$

$$H_y = \frac{-j\gamma}{\mu_\circ \omega} \left(E_+ e^{-\gamma z} - E_- e^{\gamma z}\right) \tag{2.8}$$

The first term of the equation (2.7), that is, $E_+ e^{-\gamma z}$ is known as progressive wave because it represents a wave which is traveling towards positive z. Conversely, the second term is known as regressive wave because it is a wave that travels in the opposite direction. If there are only progressive waves and electric field is divided by magnetic field, this will define the characteristic impedance for this material. Its expression is:

$$\eta = \frac{j\,\omega\mu_\circ}{\gamma} \tag{2.9}$$

With this new definition, the magnetic field can be expressed as:

$$H_y = \frac{(E_+ e^{-\gamma z} + E_- e^{\gamma z})}{\eta} \tag{2.10}$$

Once the expressions for both electric and magnetic fields are available, the power density vector, known also as Poynting vector or S_{av}, can be calculated as follow:

$$\bar{S}_{av} = \frac{1}{2} Re\ (\bar{E}\ X\ \bar{H}^*) \tag{2.11}$$

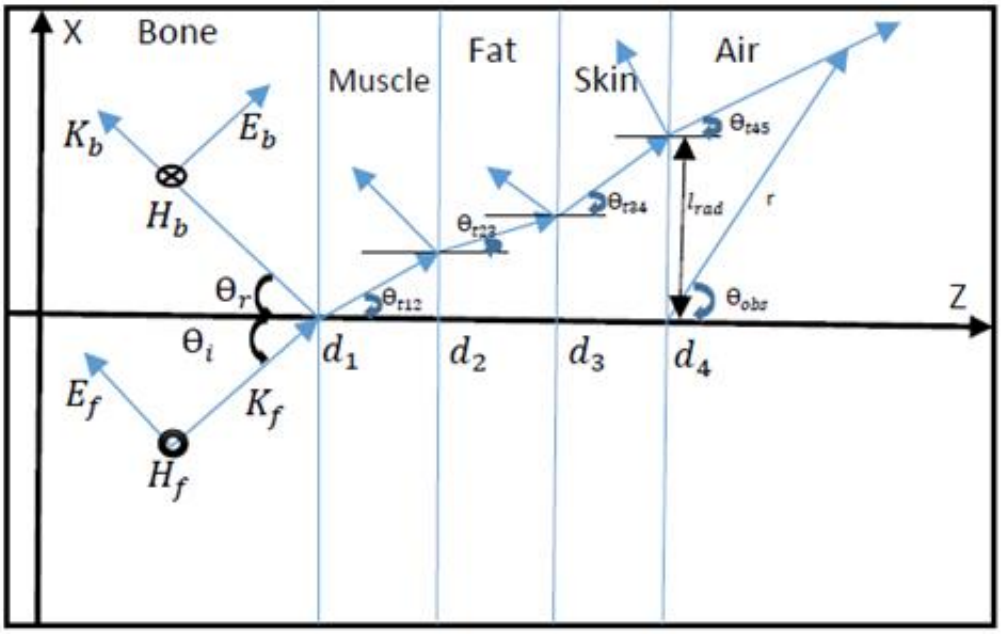

Figure 3. Multilayer human tissue model

2.2 Normal incidence of EM wave

When the EM wave travelling from one medium into another, it will be partly reflected and partially transmitted at the boundary between the two mediums. The amount of the wave that is reflected or transmitted is governed by the constitutive parameters (permittivity ε, permeability μ, and conductivity σ) of the two media.

Considering the EM wave propagates along the z direction and incidents normally on the interface between the two media:-

The incident electric and magnetic fields

$$\bar{E}_i(z) = E_{io} e^{-\gamma 1 Z}\, \hat{a}_x \tag{2.12}$$

$$\bar{H}_i(z) = H_{io} e^{-\gamma 1 Z} \hat{a}_y = \frac{E_i}{\eta_1}\, e^{-\gamma 1 z}\, \hat{a}_y \tag{2.13}$$

The reflected electric and magnetic fields

$$\bar{E}_r(z) = E_{ro} e^{\gamma 1 Z}\, \hat{a}_x \tag{2.14}$$

$$\bar{H}_r(z) = -H_{ro}e^{\gamma 1Z}\ \hat{a}_y = -\frac{E_{ro}}{\eta_1}e^{\gamma 1z}\ \hat{a}_y \tag{2.15}$$

The electric and magnetic fields transmitted to the second medium

$$\bar{E}_t(z) = E_{to}e^{-\gamma 2Z}\hat{a}_x \tag{2.16}$$

$$\bar{H}_t(z) = H_{to}e^{-\gamma 2Z}\ \hat{a}_y = \frac{E_{to}}{\eta_2}e^{\gamma 2z}\ \hat{a}_y \tag{2.17}$$

The total electric and magnetic fields in the first layer is composed of the incident and reflected fields while in the second layer it is the transmitted field only. Applying the boundary conditions at the interface of the two media for the continuity of the tangential components of the fields we get the reflection coefficient Γ and transmission coefficient T at the boundary as:

$$\Gamma = \frac{E_{ro}}{E_{io}} = \frac{\eta_2 - \eta_1}{\eta_2 + \eta_1} \tag{2.18}$$

$$\mathrm{T} = \frac{E_{to}}{E_{io}} = \frac{2\eta_2}{\eta_2 + \eta_1} \tag{2.19}$$

The normal incidence can be used in the applications that require bidirectional communications like heart pacemakers. The pacemaker needs to be programmed and setting adjustments after it is implanted within the body. This is achieved by communication with an external device. There are applications that the normal incidence of the EM wave is not valid like the proposed application in this study, monitoring of bone fracture healing, the human tissue model in this application includes an oblique layer.

2.3 Range of oblique incident angles on the multilayered model

Several researchers investigated on-body propagation and normal incidence of EM wave on human tissues [11], [31]-[33], but the existing reports on oblique incidence and its applications are limited. To the best of our knowledge, this is the first study

that expresses the range of the in-to-out incident angles for different positions of the implant and its effect on the body communication channel and on the required specification of the implanted antenna in the stated frequency range. Also, we could not trace any study in monitoring the femoral shaft or humerus fracture healing by an implanted antenna within the human body.

The goal of this section is to identify the range of incident angles that produces output transmission from the last interface out of the body [33].

At the boundaries of bone-muscle, muscle-fat, fat-skin, skin-air the incident EM wave is partly reflected and partly transmitted. The relation between incident and transmitted angles on one interface follows Snell's law of refraction [34].

$$\beta_i \sin\theta_i = \beta_{i+1} \sin\theta_t \tag{2.20}$$

Where β_i is the phase constant of the i_{th} layer. This phase constant is characterized by the constitutive parameters of the tissues and the frequency of operation. θ_i and θ_t are the incident and transmission angles of the wave respectively. In the cases when $\beta_i \leq \beta_{i+1}$ the maximum incident angle from the i_{th} layer to $(i+1)_{th}$ layer is 90° and the transmission angle always exists. In case of $\beta_i \geq \beta_{i+1}$ the maximum incident angle can be calculated from:

$$\theta_i = sin^{-1}\left[\frac{\beta_{i+1}}{\beta_i}\sin\theta_t\right] \tag{2.21}$$

$$\theta_{i_{max}} = sin^{-1}\left[\frac{\beta_{i+1}}{\beta_i}\right] \tag{2.22}$$

There is a limit for the incident angle to guarantee a partly transmitted EM wave to the next layer, otherwise the wave will be completely reflected (θ_i must be less than $\theta_{i_{max}}$). The complete reflection at one interface occurs if the incident angle is

greater than the maximum value which leads to prevent the transmission of wave out of the body and block the communication with the monitoring or controlling device. Achieving a transmission out of the body depends on the tissue properties and the incident angle on the first interface following Snell's law. This incident angle is the basis for EM wave propagation through the model. The incident angle at the first interface must be kept less than the lowest value of the maximum incident angles at all following interfaces. Practical wise, directing a narrow radiation beam of the implanted antenna at higher angle will not produce output transmission.

The maximum incident angle of the EM wave on multilayer human tissue that can achieve transmission from the last layer to outside the body depends on the properties and the arrangement of the layers so the value of the maximum in-to-out incident angle is different from the out-to-in incident angle and also according to the position of the implant in the body.

2.4 Classifications of coverage area regarding the angle of transmission

In case of IMD in human body the propagation of the EM wave from the implanted antenna is not limited to a certain angle of incidence on the human tissue but we can speak about the radiation beam of the antenna and angle of radiation or half power beam width (HPBW). We can classify the output transmission and output coverage area into three cases as follows:

First, if the angle of radiation of the antenna is equal to the maximum incident angle, this means that the radiation is taking place from 0° to the maximum angle and the transmission out of the body is from 0° to 90° which is the maximum coverage area of transmission outside the body. *Second*, if the angle of radiation of the antenna is lower

than the maximum incident angle, then the output transmission coverage angle is lower than 90° and the coverage area is lower than the first case. *Third*, if the radiation angle of the antenna is higher than the maximum incident angle, in this case the output coverage area is at its maximum value as in the first case but unwanted radiation in the human body will be reflected at the tissue interfaces and may increase the specific absorption rate (SAR) and increase the tissue's temperature. So one of the suggested future work of this study is to demonstrate the importance of specifications and type selection of the implanted antenna according to the position of implant for a satisfactory level of SAR with respect to the standards within human tissue.

Table 1. Transmission through bone, muscle, fat, skin to air (4 layers)

	400 MHz	**900 MHz**	**2.4 GHz**	**6 GHz**	**10 GHz**
$\boldsymbol{\theta_{in-out_{max}}}$	15.818°	16.352°	17.082°	18.517°	19.997°
$\boldsymbol{\theta_{out_{max}}}$	90°	90°	90°	90°	90°
$\boldsymbol{P_{l_{max}}}$ **(mm)**	58.8	58.8	58.8	58.7	58.7
$\boldsymbol{l_{rad_{max}}}$**(mm)**	11.2	11.3	11.1	10.8	10.6

Table 2. Transmission through muscle, fat, skin to air (3 layers)

	400 MHz	**900 MHz**	**2.4 GHz**	**6 GHz**	**10 GHz**
$\boldsymbol{\theta_{in-out_{max}}}$	**7.280°**	**7.638°**	**7.854°**	**8.176°**	**8.592°**
$\boldsymbol{\theta_{out_{max}}}$	90°	90°	90°	90°	90°
$\boldsymbol{P_{l_{max}}}$ **(mm)**	57.3	57.3	57.2	57.2	57.2
$\boldsymbol{l_{rad_{max}}}$**(mm)**	10.8	10.6	10.5	10.5	10.3

Table 3. Transmission in case of oblique fractured bone

	400 MHz	**900 MHz**	**2.4 GHz**	**6 GHz**	**10 GHz**
$\boldsymbol{\theta_{in-out_{min}}}$	29.183°	28.648°	27.918°	26.483°	25.003°
$\boldsymbol{\theta_{in-out_{max}}}$	45°	45°	45°	45°	45°
$\boldsymbol{P_{l_{max}}}$ **(mm)**	59.6	59.6	59.5	59.4	59.3
$\boldsymbol{l_{rad_{max}}}$**(mm)**	10.7	10.7	10.6	10.2	9.9

The maximum incident angle on the bone to muscle interface is $\theta_{in-out_{max}}$. This angle achieves maximum transmission angle $\theta_{out_{max}}$ from the skin to air outside the body. The maximum propagation path length $P_{l_{max}}$ of the EM wave through the tissue layers is the total distance travelled by the wave within the body, and the maximum length at the last layer from which the EM wave can radiate out of the body is $l_{rad_{max}}$. All parameters are shown in Figure 3. Table 1 shows the calculated values at some common frequencies in the MICS and ISM bands when the transmission is through 20 mm bone, 27.5 mm muscle, 8.5mm fat, 1.5 mm skin to air (4 layers model). $P_{l_{max}}$, and $l_{rad_{max}}$ are given by:

$$P_{l_{max}} = d_1 \sec\theta_{max_{i12}} + (d_2 - d_1)\sec\theta_{t12} + (d_3 - d_2)\sec\theta_{t23} + (d_4 - d_3)\sec\theta_{t34} \quad (2.23)$$

$$l_{rad_{max}} = d_1 \tan\theta_{max_{i12}} + (d_2 - d_1)\tan\theta_{t12} + (d_3 - d_2)\tan\theta_{t23} + (d_4 - d_3)\tan\theta_{t34} \quad (2.24)$$

Table 2 lists the results that correspond to transmission through muscle, fat, skin to air (3 layers model). It should be mentioned that the maximum out-to-in angle is always 90° because $\beta_{air} < \beta_{skin}$ in the whole frequency range.

The results of maximum incident angles when the wave propagation starts from bone is almost double the corresponding values when it starts from muscle. It is remarkable in the three and four layers cases that as the incident angle increases, we have to

increase the operating frequency to guarantee the transmission of EM wave outside the body. Propagation path length inside the tissue and radiating length at the last layer is slightly higher in case of transmission starting from bone to outside the body.

The results in case of 45° oblique fractured bone are shown in Table 3. The incident angle in this case is measured from the perpendicular plane to the first bone-fracture interface as will be discussed in section (4.5). It should be noted that the normal incident on the fracture layer produces an oblique transmission from the fracture to the following bone layer and oblique incident on the bone-muscle interface. The maximum allowed incident angle on the bone-fracture interface is 45° which produces a normal incidence on the following interfaces and normal transmission out of the body.

As provided by the results, the maximum incident angles in cases of three and four layers model are small angles lead to 90° transmission angle from the skin tissue to air. A small change in the incident angle results in a larger change in the transmission angle from the last tissue layer, so controlling the antenna beam is important to avoid unwanted radiation within the body and keep output transmission to the monitoring device.

The observation angle θ_{obs} is measured at the point of observation from the z-axis to x-axis as in Figure 3 and the distance l_{rad} from the z-axis to the point at which the EM wave is transmitted out of the body. When the measurement is taken at distance r from the skin, the relation between the transmission angle and observation angle is provided by the following formula:

$$\theta_{obs} = sin^{-1}\left[\frac{l_{rad}}{r\sqrt{1+tan^2\theta_t}}\right] + \theta_t \quad (2.25)$$

Where θ_{obs} angle measured from the z axis to the point of observation, r is the distance outside the body at which the measurement of average power density is taken.

All the results and calculations are totally carried out by codes written in MATLAB and the electrical properties of the tissues are from [35].

Chapter 3

ANTENNA WITHIN HUMAN BODY

The human body's characteristics play the key role in designing the implanted antenna for biomedical applications. The lossy behavior of the human tissues affects the performance of the antenna and the EM wave propagation through the tissue. The biological tissue variation between patients add extra complexity in finding the suitable design of the implanted antenna.

Implanted antennas are located within tissues in two ways. As shown in Figure 4, one way is that an implanted antenna is coated by an ultrathin insulation material before contacts the biological tissue as in our study in this thesis. The other is that an antenna contacts a biological tissue using a buffer layer as in capsule endoscope. The buffer layer of Figure 4(b) can be an air region or a dielectric material. The antenna of Figure 4(a) requires smaller space in a human body than that of Figure 4(b), but the link of the former generates higher SAR value because of the direct contact and there is a need to reduce the excitation signal of the antenna to satisfy the SAR standards and safety precautions of tissue [36].

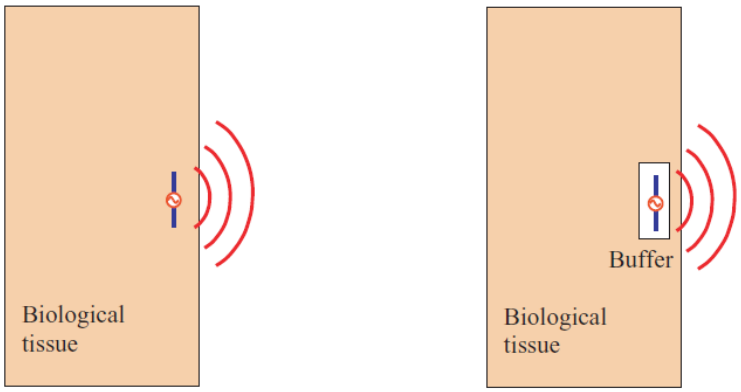

(a) (b)

Figure 4. Antenna in biological tissue: (a) coated antenna, (b) Antenna in buffer

3.1 Antenna characteristics within human body

The characteristics of antennas, which are surrounded by lossy tissues is different from the antennas in air or free space. The lossy tissue results in a different wavelength and introduces conduction current. Many parameters (e.g. wave number, attenuation constant, phase constant, intrinsic impedance, etc.) that are real in free space become complex in a lossy medium [37]. Therefore, different characterization methods of body-matched antenna such as reflection coefficient, bandwidth, efficiency, and radiation pattern are provided in the following section, some of those definitions are modified for antennas in lossy medium.

3.1.1 Impedance and reflection coefficient

Figure 5 shows a transmitting antenna fed with line of characteristic impedance Z_o. The impedance of the antenna is characterized by the ohmic losses resistance R_l and radiation resistance R_{rad} and the reactance X_A.

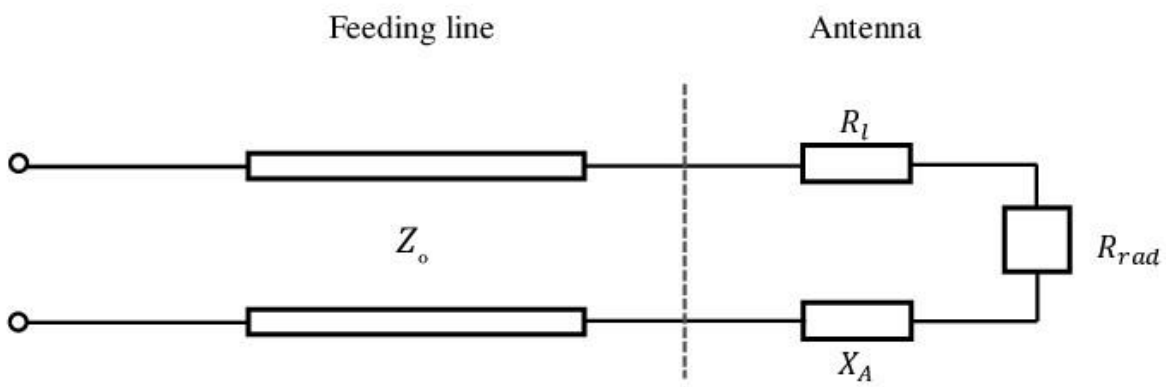

Figure 5. Equivalent circuit of antenna and feeding line.

The total impedance of the antenna Z_A is expressed as:

$$Z_A = R_l + R_{rad} + jX_A \tag{3.1}$$

The power density in the lossy human tissue can be written as:

$$S_l = \text{Re}\left(\frac{|\bar{E}|^2}{\eta} e^{-2\alpha r} \right) \tag{3.2}$$

Where α is the attenuation constant, η is the intrinsic impedance of the medium, the exponential term represents the decay or the wave while propagating in the r direction.

The radiation resistance of the antenna in term of the radiated power and the input current I is:

$$R_{rad} = \frac{\oiint S_l \sin\theta \, r^2 \, d\theta \, d\varphi}{I^2} \tag{3.3}$$

The current distribution of the antenna is altered due to the presence of the lossy medium, and then the radiation resistance is different compared with the value in free space.

The antenna efficiency η_e and the reflection coefficient Γ are expressed by:

$$\eta_e = \frac{R_{rad}}{R_{rad} + R_l} \tag{3.4}$$

$$\Gamma = \frac{Z_A - Z_o}{Z_A + Z_0} \tag{3.5}$$

To achieve a low reflection coefficient, it is required to match the impedance of the power source with that of the antenna. Ideally, the line impedance Z_o must be complex conjugate of the antenna impedance Z_A.

3.1.2 Radiation pattern of the antenna

The radiation pattern or antenna pattern refers to the directional dependence of the radio wave strength from the antenna. It is referred to the angles θ and φ and the electric field strength at constant distance r from the antenna as follow:

$$C\ (r,\theta,\varphi) = \frac{|E\ (r,\theta,\varphi)|}{|E\ (r,\theta,\varphi|_{max}} \tag{3.6}$$

The electromagnetic field radiated by an antenna can be simplified into three characteristic regions depending on the distance from the antenna: reactive near-field, radiating near-field and far-field. The reactive near-field which is known as "Rayleigh zone" is caused by charges and currents on the antenna. Increasing the distance to the antenna (Fresnel distance R_{nf}), the radiation fields (Fresnel zone) begin but still depend on the distance to the antenna. At a certain distance away from the antenna, the radiated E-fields and H-fields are not affected by the charges and currents. This range is called far-field (Fraunhofer zone) and the corresponding distance is termed as Fraunhofer distance R_{ff}. In the far field, the radiated wave of the antenna can be considered as a plane wave. E-fields and H-fields are in phase and the antenna pattern at this region does not depend on the distance. These three different ranges can be determined by the dimension of the antenna D_A and wavelength λ_m as follows

Reactive near field $r_A \leq \frac{\lambda_m}{2\pi}$

Radiative near field $\frac{\lambda_m}{2\pi} \leq r_A \leq \frac{2\ D_m^2}{\lambda_m}$

Far field $r_A \geq \frac{2\,D_m^2}{\lambda_m}$

The human body matched antennas may operate in the near field or far field range. In this thesis we are interested in the far field of the implanted antenna within human body for health care monitoring applications.

3.1.3 Specific absorption rate SAR

The Specific Absorption Rate (SAR) is a measure of the absorption of EM waves within human tissues by heat conversion per unit mass in W/kg.

$$\text{SAR} = \frac{|E|^2 \sigma}{\rho} \tag{3.7}$$

The parameters used in calculating the SAR value in equation 3.7 are the RMS value of the electric field E, the conductivity σ and the mass density ρ of the medium. The standards set a limit for the averaged SAR value over a mass of 1g, or 10 g of the tissue. The SAR limits are calculated on the basis that a temperature rise of 1 C° in a resting person due to radiation is considered harmful. According to this restriction, technical organizations define maximum SAR values for wireless devices as follows: The federal communication commission FCC in USA specifies a maximum SAR of 1.6 W/kg in a cube of 1 g of tissue.

The European committee for electro-technical standardization CENELEC in European Union specifies a limit of 2 W/kg averaged SAR over a 10 g cube.

The SAR value in human tissue is very important parameter when designing an implanted antenna to guarantee that the antenna is safe for the body.

3.1.4 Polarization

The radiated EM waves from the antenna in the far-field consist of two orthogonal components: the electric and magnetic field vectors, which oscillate harmonically. The polarization of the EM waves describes the time varying direction and relative magnitude of the EM waves (normally referred to as the E-field). Polarization can be classified as linear, circular or elliptical. In this thesis only linear polarization is considered. The field is linearly polarized, when the electric field vector is always along a certain axis.

3.1.5 Miniaturization

Implantable medical devices usually need a certain degree of miniaturization to facilitate their placement and for the patients' comfort. As the antenna occupy a considerable area of the IMD, antenna miniaturization is one of the most important characteristics in the design of implantable antennas. The main goal of the miniaturization is to reduce the antenna size at a certain operating frequency while keeping the efficiency of it at an accepted level. Radiation pattern and bandwidth are also affected by the size reduction of the antenna.

Several techniques are presented in literatures for the design of implantable antennas. Antenna design based on batch radiator like planar inverted F antenna PIFA and multilayer PIFA structures emerge as commonly used structures for implantable antennas of small volume. Other radiator structures like monopoles, dipoles and loop antennas are also presented in literatures.

Lengthening the current flow pass on the patch surface in a smaller space is another technique of miniaturization. Fractal and spiral geometries have been investigated for this purpose. Another technique for miniaturization of implantable antenna is to use

dielectric substrate with high permittivity. Increasing the operating frequency can also help in miniaturization of antenna as the wavelength will decrease but this increase in frequency affects the penetration of EM wave through the tissue and the absorption of electric field as heat.

3.1.6 Bandwidth

The bandwidth identifies the frequency spectrum where the antenna is matched and the provided power is radiated (minus the losses due to the radiator itself).

In order to understand the main characteristics of antennas surrounded by lossy media, let us consider the following power expression:

$$P_{sourse} = P_{rad} + P_{abs} \tag{3.8}$$

Where P_{source} is the source power, P_{rad} is the radiated power from the antenna, and P_{abs} is the absorbed power in the tissue surrounding the antenna.

When considering sources in lossy media as the case of human tissue, the near field terms of the electromagnetic field strongly dissipate in the surrounding environment. Therefore, P_{abs} can be much higher than P_{rad}, and can be almost equal to P_{source}. Most of the provided power is absorbed by the body regardless the efficiency of the radiator, a small percentage of P_{source} is actually reflected back to the generator. This may result in unusually wide band behaviors.

3.2 Half wave dipole antenna

The half-wave dipole antenna is a very commonly used antenna. It is an antenna constructed using a conductive wire or metallic part that has a length equal to the electrical half wavelength of the operating frequency.

The excitation to the half wave dipole antenna is delivered at the center. So, it can be said that the feeding to the dipole is presented at the quarter wavelength point. It is a linear current whose amplitude varies as one-half of a sine wave with a maximum at the center of the antenna. The structure of the antenna is shown in Figure 6.

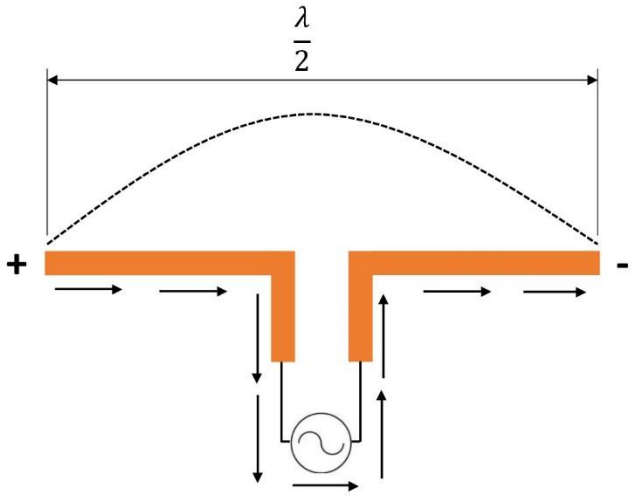

Figure 6. Structure of half wave dipole antenna.

3.2.1 Half wave dipole receiving antenna

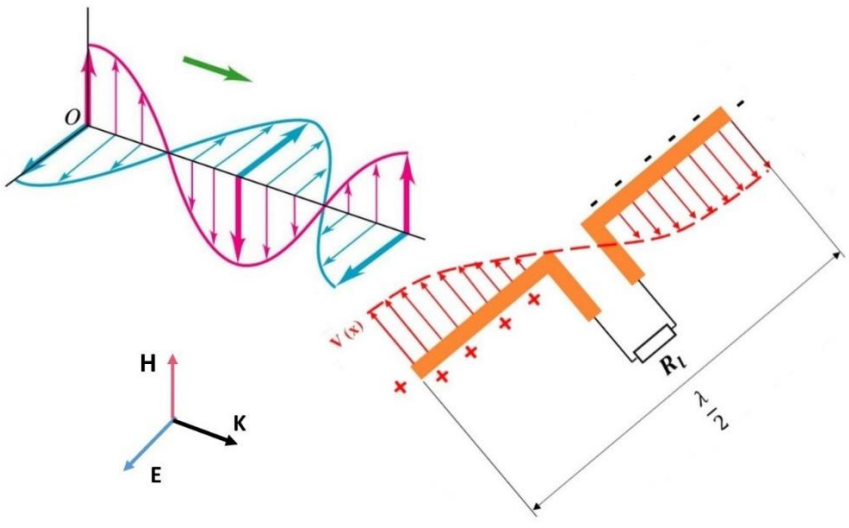

Figure 7. Receiving half wave dipole.

Figure 7 shows the propagating EM wave in addition to the two conducting parts of the receiving antenna. The coming time varying radio signal pushes the electrons forward and backward in the conducting parts, which charges the ends with alternative positive and negative charges. This process induces a standing wave of voltage and current along the antenna. The current then flows down through the transmission line to the receiver. The phase of the voltage at the transmission line would be reversed, since the receiver absorbs energy from the antenna.

3.2.2 Half wave dipole transmitting antenna

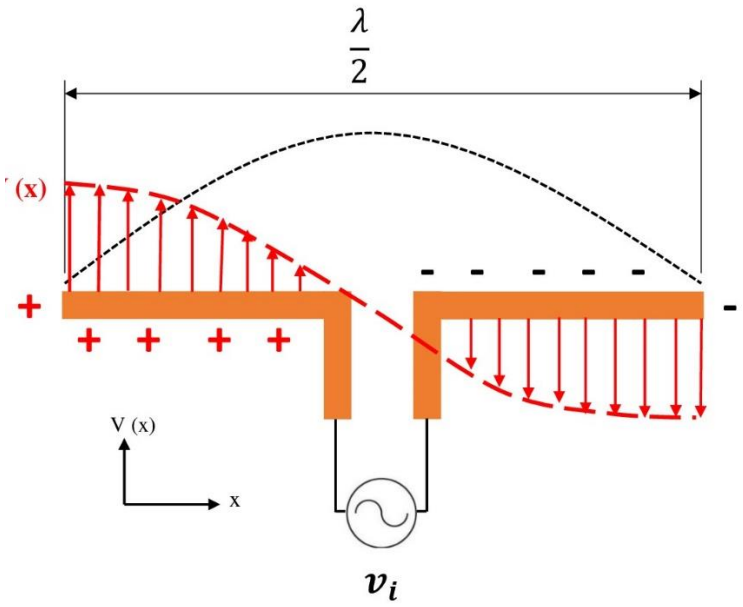

Figure 8. Transmitting half wave dipole antenna.

The transmission line applies an oscillating voltage from the transmitter to the antenna, driving a sinusoidal oscillation. Since the antenna is fed at its resonant frequency, the input voltage is in phase with the current, so the antenna presents a pure resistance to the feedline thus eliminating the need for tuning to achieve a conjugate impedance

match. The energy from the driving current provides the energy radiated as radio waves. Figure 8 shows the voltage and current distribution on the transmitting antenna.

Practical wise, to obtain a resonant condition for a half-wave dipole, the physical length must be somewhat shorter than a free space half-wavelength, and as the antenna wire thickness is increased, the length must be reduced more to achieve resonance.

3.2.3 Radiation pattern

The electric and magnetic field distribution when the antenna is placed along the z-axis and for the half-sine wave current on the half-wave dipole can be expressed as:

$$E_\theta \simeq j\eta \frac{I_o e^{-jkr}}{2\pi r}\left[\frac{\cos\left(\frac{\pi}{2}\cos\theta\right)}{\sin\theta}\right] \tag{3.9}$$

$$H_\varphi \simeq j \frac{I_o e^{-jkr}}{2\pi r}\left[\frac{\cos\left(\frac{\pi}{2}\cos\theta\right)}{\sin\theta}\right] \tag{3.10}$$

And the time average power density is given by:

$$W_{av} = \eta \frac{|I_o|^2}{8\pi^2 r^2}\left[\frac{\cos\left(\frac{\pi}{2}\cos\theta\right)}{\sin\theta}\right]^2 \simeq \eta \frac{|I_o|^2}{8\pi^2 r^2} Sin^3\theta \tag{3.11}$$

The average power intensity is

$$U = r^2 W_{av} = \eta \frac{|I_o|^2}{8\pi^2}\left[\frac{\cos\left(\frac{\pi}{2}\cos\theta\right)}{\sin\theta}\right]^2 \simeq \eta \frac{|I_o|^2}{8\pi^2} Sin^3\theta \tag{3.12}$$

Figure 9 shows the 3D and 2D far field patterns of the half wave dipole antenna at 900 MHz in free space when the antenna is placed along the z axis. The pattern is omnidirectional in the x-y plane and zero in the z axis. The patterns are obtained by CST simulator.

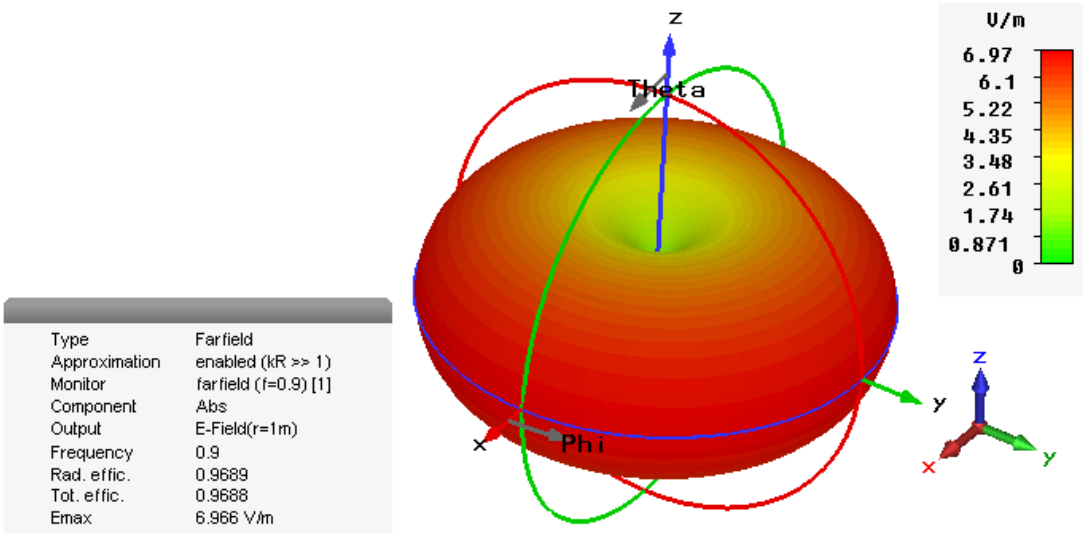

(a) 3D pattern

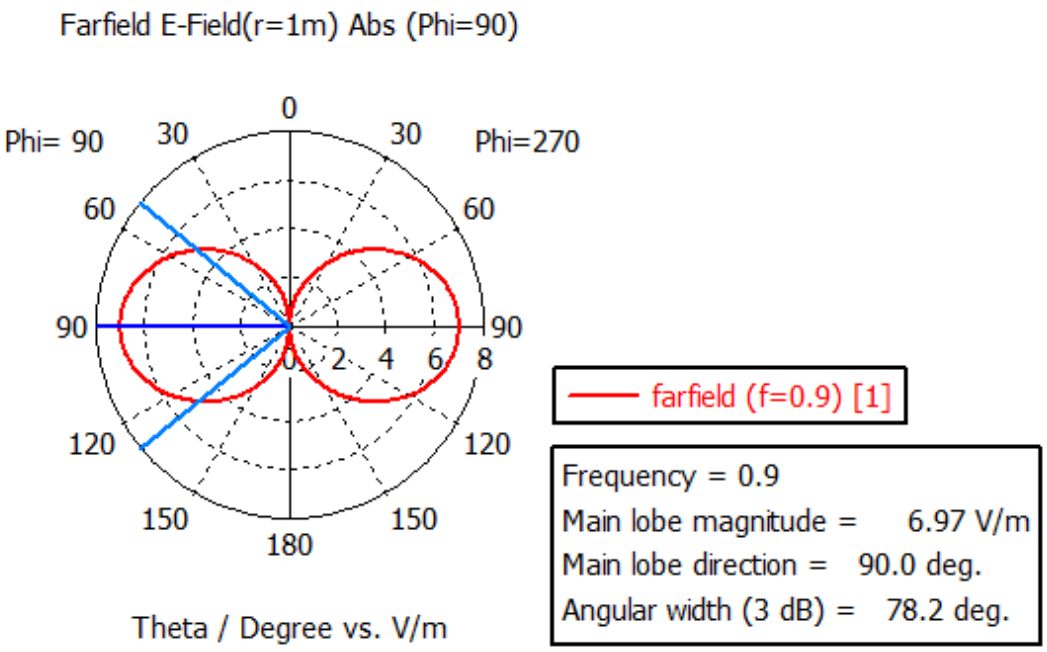

(b) 2D pattern

Figure 9. Radiation pattern of half wave dipole at 900 MHz (a) 3D pattern, (b) 2D pattern

3.2.4 Effect of lossy medium surrounding the antenna

In this section we compare the performance of the half wave dipole antenna when placed in free space and when it is implanted within a lossy human tissue like fat and muscle at 900 MHz which is one of our frequencies of interest in this thesis. CST Microwave Studio is used for this comparison.

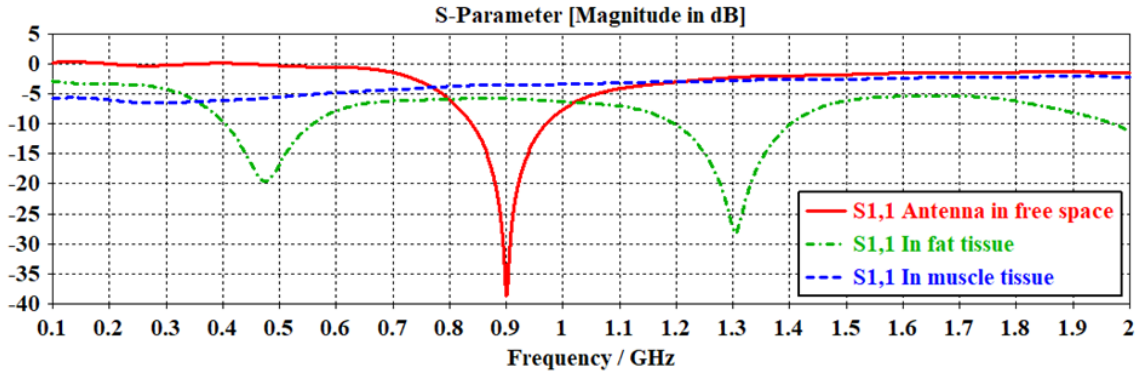

Figure 10. Return loss of the antenna when placed in air and in lossy tissue.

At 900 MHz, the half wavelength of the antenna in air is 166.55 mm. The antenna is expected to resonate at length 0.47 of the wavelength. In this simulation the resonance length at the selected frequency was 153.55 mm gave return loss of -38.8 dB. When the antenna is placed in the lossy tissues, the electric field value become lower than its value in free space and it experienced a considerable decay in the return loss and both of radiation efficiency and total efficiency. Figure 10 shows the simulated return loss of the antenna when it is placed in free space, fat, and muscle tissue. The antenna needs to be tuned in length according to the lossy tissue's electrical properties to resonate at the selected frequency. This operation of the antenna in the proposed healthcare monitoring application will be discussed in Chapter 5. Table 4 summarizes the results in the lossless and lossy tissues in the far field of the antenna and the maximum electric field in the main lobe direction at $\theta° = 90°$, and $\varphi = 90°$.

Table 4. Antenna performance in air and in lossy tissue

Medium	Total efficiency	Maximum electric field V/m
Free space	0.9688	6.966
Fat tissue	0.2856	3.915
Muscle tissue	0.004439	0.5005

3.2.5 Effect of 2D miniaturization on implanted Antenna performance

The straight line wire antenna is one of the most common antenna structures. The research for small and efficient antennas results in the creation of a variety of antennas as Helix, Koch fractal, Hilbert curve fractal, and meander antenna. This study focuses on the meander antenna as it is the most suitable to be implanted in the available space of the proposed health care application.

Meander line technique allows designing antennas with a small size and provides wideband performance. Meander line antenna is an interesting class of resonant antennas and they have been widely studied in order to reduce the size of the radiating elements in wire antennas: monopole, dipole and folded dipole type antennas. In meander line antenna the wire is continuously folded intended to reduce the resonant length [38].

In this section we study the effect of antenna miniaturization by meandering technique on the performance of the implanted antenna in human femur at 900 MHz. The meander technique for miniaturization is selected due to its suitability for implanting within the model under investigation. The human femur model is a multilayered cylindrical model consists of cylindrical bone followed by muscle, fat and skin. Figure 11 shows the return loss comparison of the straight antenna and the antenna

miniaturized by meander technique. Table 5 summarizes the performance results of both antennas and the maximum electric field in the main lobe direction.

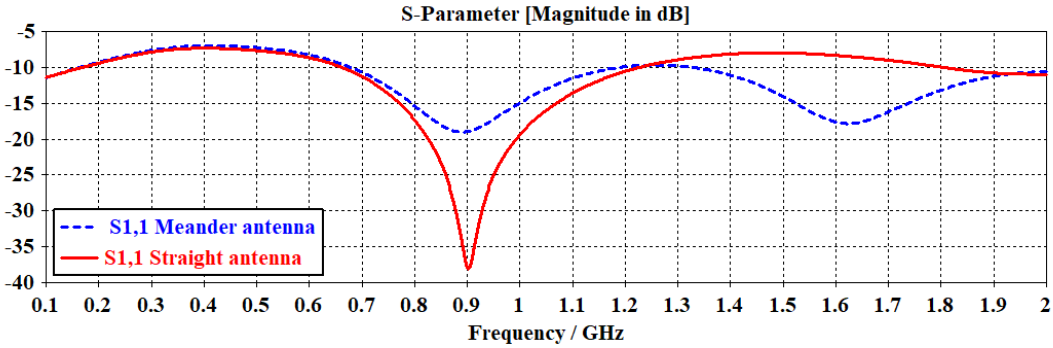

Figure 11. Return loss of line and meandered implanted antenna in tissue

Table 5. Performance of meander and line implanted antennas.

Antenna topology	Total efficiency	Maximum electric field V/m
Straight	0.009545	0.3308
Meander	0.006296	0.2699

3.3 Advantages and disadvantages of half wave dipole antenna

Advantages

The advantages of half wave dipole antenna are as follows:

- Simple design and implementation.
- Simple fabrication on PCB.
- Can be miniaturized by simple miniaturization techniques so it can work well at low frequencies.
- Suitable geometry to be implanted in different position within human body.
- These antennas do not show sensitivity to input impedance.
- The length of the antenna is appropriate for the free space characteristics with the operating frequency.
- The antenna is not bulky.

- It is cost-efficient.
- The input impedance of this dipole antenna properly matches with the impedance of the transmission line.

  These advantages are the reasons of our interest in the half wave dipole in this thesis.

Disadvantages.

The disadvantages are given below:

- It is not majorly used as an independent antenna and thus is used as the basic element for other antennas that operate at very high frequencies.
- The radiation pattern is of omnidirectional nature thus the directivity offered by it is of concern within the body with respect to unwanted radiation in some positions.

Chapter 4

HEALTHCARE MONITORING APPLICATION

Monitoring of bone fracture healing

When most tissues, such as those of the skin, muscles, and internal organs, are significantly injured, they mend themselves by producing scar tissue to replace the injured tissue. The scar tissue often looks different from normal tissue or interferes with function in some way. In contrast, bone heals by producing actual bone tissue.

When a bone heals itself after a fracture, the fracture often eventually becomes virtually undetectable. Even bones that have been shattered, when treated appropriately, can often be repaired and function normally. This point attracts the attention to the good monitoring of bone during the healing period.

This study focuses on the monitoring of femoral shaft and upper arm fractures healing. Our goal is to ease the patient's life during the long treatment period and to avoid repeated exposing to X-Ray radiation of traditional monitoring. Femoral shaft fractures result from significant force transmitted from a direct blow or from indirect force transmitted at the knee. These may be the result of bone weakness from osteoporosis or lytic lesion [39].

4.1 Types of shaft fractures

Shaft fractures vary greatly, depending on the force that causes the break. The pieces of bone may line up correctly (stable fracture) or be out of alignment (displaced fracture). The skin around the fracture may be intact (closed fracture) or the bone may puncture the skin (open fracture).

The most common types of shaft fractures include: Transverse fracture, in this type of fracture, the break is a straight horizontal line going across the shaft as in Figure 12 (a). Oblique fracture, this type of fracture has an angled line across the shaft and is shown in Figure 12 (b) for stable oblique fracture, (c) for displaced oblique fracture. Figure 12 (d) shows the Spiral fracture, the fracture line encircles the shaft like the stripes on a candy cane. A twisting force to the bone causes this type of fracture. Comminuted fracture, in this type of fracture, the bone has broken into three or more pieces as indicated by Figure 12 (e). In most cases, the number of bone fragments corresponds to the amount of force needed to break the bone [40].

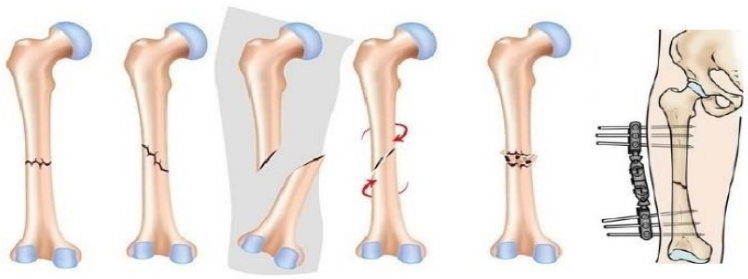

(a) (b) (c) (d) (e) (f)

Figure 12. Bone fracture types (a) Transverse fracture, (b) Stable oblique fracture, (c) Displaced oblique fracture, (d) Spiral fracture, (e) Comminuted fracture, (f) Surgical fixation of fracture.

This study focuses on the oblique and transverse fractures of bone. These types of fractures are treated by different surgeries, either internal or external, to hold the bones in place while they heal. The most common surgery for a broken femur is called intramedullary nailing. This surgery inserts a rod into the length of the bone with screws above and below to hold it into place. Figure 1 (f) shows the shaft fracture and the surgical fixation module.

4.2 Bone healing process

The bone healing process is the same in all broken bones. This is true whether a bone has been cut as part of a surgical procedure or fractured through an injury.

The bone healing process has three corresponding stages: inflammation, bone production and bone remodeling as shown in Figure 13.

(a) (b) (c)

Figure 13. Bone healing process (a) Inflammation, (b) Production, (c) Remodeling

- **Inflammation** process starts immediately after the bone is fractured and continues for several days. When the bone is fractured, there is bleeding into the area, leading to inflammation and clotting of blood at the fracture site. This provides the initial structural stability and framework for producing new bone.
- **Bone production** begins when the clotted blood formed by inflammation is replaced with fibrous tissue and cartilage which is known as soft callus. As healing progresses, the soft callus is replaced with hard bone (known as hard callus), which is visible on x-rays several weeks after the fracture.

- **Bone remodeling,** the final phase of bone healing, goes on for several months. In remodeling, bone continues to form and becomes compact, returning to its original shape. In addition, blood circulation in the area improves. Once suitable bone healing has occurred, weight bearing (such as standing or walking) encourages bone remodeling.

During the healing process, the electrical properties of the fracture layer change gradually from the blood to the normal bone properties.

4.3 Importance of continuous monitoring of healing

In some cases, fractured bones do not grow back together as expected. They may

- Not grow back together (non-union).
- Grow back together very slowly (delayed union)
- Grow back in the wrong position (mal-union)

These problems are more likely to occur when

- The broken bones are not kept next to each other and are not kept from moving or not restrained with a cast or a splint.
- The blood supply is disrupted.

Early diagnosis of these problems is obtained by continuous monitoring of the fracture healing from the beginning of treatment.

4.4 Fractures' healing follow up

The most common way to evaluate a fracture is with X-Ray, which provides clear images of bone. X-Rays are linked to a slightly increased risk of cancer. Exposure to

high radiation levels can have a range of effects, such as vomiting, bleeding, and fainting.

In cases of traumatic femur fractures, schedule a clinic follow-up visit at 2 weeks, 6 weeks, 3 months, 6 months, and 1 year with pali X-Ray is also needed. The femur fracture should be healed within 3 months [41].

From this difficult and uncomforted long period of treatment we propose the monitoring by an implanted antenna. The proposed monitoring method will not impose any extra pressure on the patient as two surgical operations must be done to insert the fixation unit and to remove it after the completeness of bone healing. So the monitoring antenna will be implanted with the first surgery and removed by the second surgery after the complete healing of bone. The difference between the transmitted average power densities out of the body in cases of fractured bone and normal bone provides information about the healing status.

By this monitoring application, no need for repeated visits to the laboratory or repeated exposing of the patient to the X-Ray during the long treatment period.

4.5 The tissue model

A simplified model of multilayer human tissues is composed of consecutive bone, muscle, fat, and skin. The model is used to observe the effect of incident angle of EM wave on the in-to-out interfaces with the output transmission angle outside the body. Two cases are considered, when the EM wave propagation is through bone, muscle, fat, skin, to air and when it is through muscle, fat skin, to air.

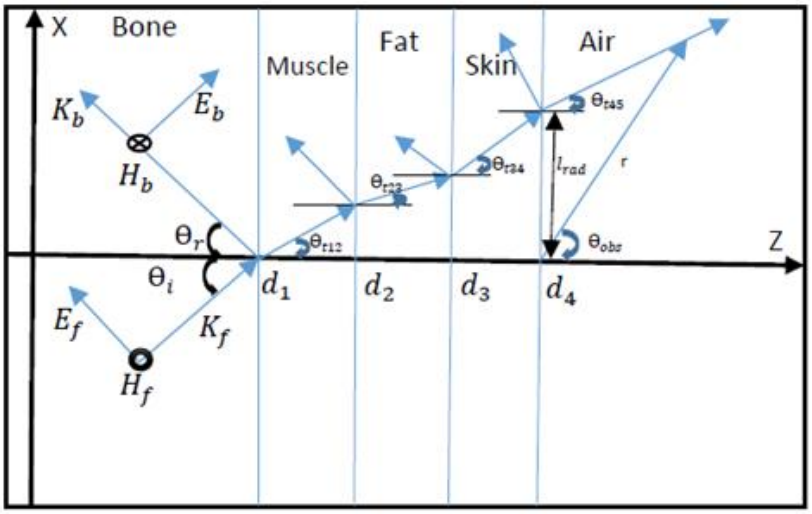

(a)

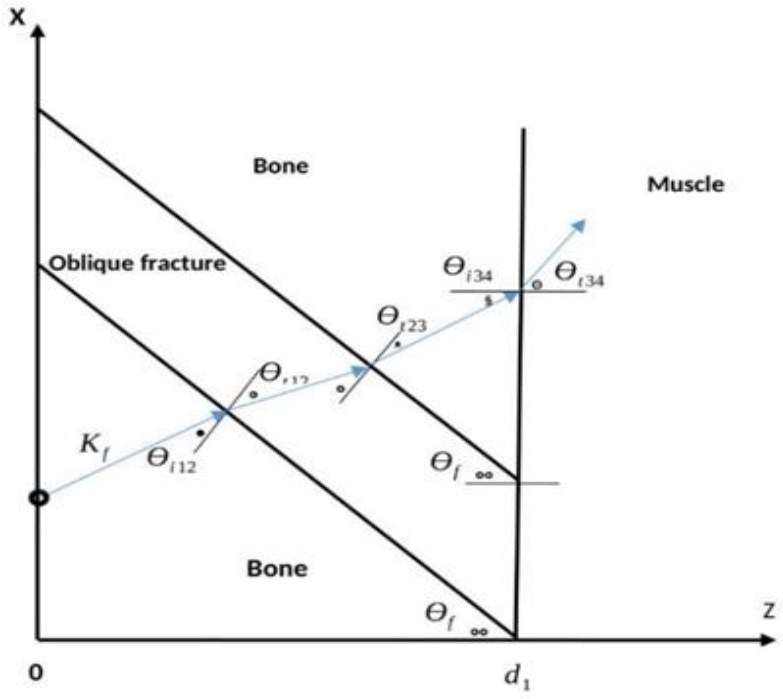

(b)

Figure 14. (a) Normal bone model, (b) Oblique fractured bone model

Figure 14 shows the model in case of normal bone (a) and oblique fractured bone (b). The normal bone model is composed of consecutive bone, muscle, fat, skin, and air layers, while a 45° oblique layer is added to the bone for representing the fracture. Due to the geometrical shape of the model, the normal incidence of EM wave from the bone layer on the bone-fracture interface will produce an oblique transmission

from fracture to the following bone layer and then oblique incidence on the bone-muscle interface. The normal propagation from in-to-out is not valid for this application and this is the reason of our interest in oblique incidence of EM wave.

4.6 Analysis of the multilayered model

A planar multilayer human tissue model is used to characterize the in-to-out body channel. The model is composed of bone, muscle, fat, skin tissues and the last layer is air at which the EM wave is transmitted outside the body. Each layer has its specific physical thickness for adults and electrical properties change according to the operating frequency. The channel characteristics are studied in two cases when the transmission is through bone, muscle, fat, skin, to air and when it is through muscle, fat, skin to air layer.

A parallel polarized plane wave is obliquely incident on the first interface as shown in Figure 2.

The total electric and magnetic fields in the i_{th} layer are given by equations (4.1), (4.2) [34], [42]

$$\bar{E}_i = E_{fi}\,(\cos\theta_i\ \hat{a}_x - \sin\theta_i\ \hat{a}_z)\,e^{-\gamma(x\sin\theta_i + z\cos\theta_i)} + E_{bi}\,(\cos\theta_i\ \hat{a}_x + \sin\theta_i\ \hat{a}_z)\,e^{-\gamma(x\sin\theta_i - z\cos\theta_i)} \quad (4.1)$$

$$\bar{H}_i = \left\{\frac{E_{fi}}{\eta_i}\,e^{-\gamma\,(x\sin\theta i + z\cos\theta_i)} - \frac{E_{bi}}{\eta_i}\,e^{-\gamma\,(x\sin\theta i - z\cos\theta_i)}\right\}\hat{a}_y \quad (4.2)$$

Where E_{fi} and E_{bi} are the amplitudes of the incident and reflected waves, θ_i is the angle of incidence, γ_i is the propagation constant and η_i is the wave intrinsic impedance of the i_{th} layer.

The propagation constant is expressed as in [34]:

$$\gamma = \alpha + j\beta \tag{4.3}$$

Where α the attenuation constant, β the phase constant and the intrinsic impedance η of the wave can be calculated in each tissue layer for the operating frequency range [11].

$$\alpha = \omega \sqrt{\frac{\mu\epsilon}{2}\left[\sqrt{1+\left(\frac{\sigma}{\omega\varepsilon}\right)^2}-1\right]} \tag{4.4}$$

$$\beta = \omega \sqrt{\frac{\mu\epsilon}{2}\left[\sqrt{1+\left(\frac{\sigma}{\mu\epsilon}\right)^2}+1\right]} \tag{4.5}$$

$$\eta = \sqrt{\frac{\mu}{\epsilon - j\left(\frac{\epsilon}{\sigma}\right)}} \tag{4.6}$$

The conductivity, permeability and permittivity of the tissue layer are denoted by σ, μ, and ϵ respectively for the radian frequency ω.

The electric and magnetic fields along the planar tissue layers are calculated from equations (4.1), (4.2) by applying the boundary conditions at the interfaces to satisfy the continuity of the tangential field components from the following equation:

$$\begin{bmatrix} A_1 & A_2 \\ A_3 & A_4 \end{bmatrix} [E] = [b] \tag{4.7}$$

Where $A_{1,2,3,4}$ are 4×4 matrices, and can be calculated as:

$$A_1 = \begin{bmatrix} e^{\gamma_1 d_1 \cos\theta_1}\cos\theta_1 & -e^{-\gamma_2 d_1 \cos\theta_2}\cos\theta_2 & -e^{\gamma_2 d_1 \cos\theta_2}\cos\theta_2 & 0 \\ \dfrac{-e^{-\gamma_1 d_1 \cos\theta_1}}{\eta_1} & \dfrac{-e^{-\gamma_2 d_1 \cos\theta_2}}{\eta_2} & \dfrac{e^{\gamma_2 d_1 \cos\theta_2}}{\eta_2} & 0 \\ 0 & e^{-\gamma_2 d_2 \cos\theta_2}\cos\theta_2 & e^{\gamma_2 d_2 \cos\theta_2}\cos\theta_2 & -e^{-\gamma_3 d_2 \cos\theta_3}\cos\theta_3 \\ 0 & \dfrac{e^{-\gamma_2 d_2 \cos\theta_2}}{\eta_2} & \dfrac{-e^{\gamma_2 d_2 \cos\theta_2}}{\eta_2} & \dfrac{-e^{-\gamma_3 d_2 \cos\theta_3}}{\eta_3} \end{bmatrix} \tag{4.8}$$

A_2 contains only two non-zero elements:

$a2_{13} = -e^{\gamma_2 d_2 \cos\theta_3} \cos\theta_3$, and $a2_{14} = \frac{e^{\gamma_3 d_2 \cos\theta_3}}{\eta_3}$

A_3 also contains two non-zero elements:

$a3_{14} = e^{-\gamma_3 d_3 \cos\theta_3} \cos\theta_3$, and $a3_{24} = \frac{e^{-\gamma_3 d_3 \cos\theta_3}}{\eta_3}$

$A_4 =$

$$\begin{bmatrix} e^{\gamma_3 d_3 \cos\theta_3}\cos\theta_3 & -e^{-\gamma_4 d_3 \cos\theta_4}\cos\theta_4 & -e^{\gamma_4 d_3 \cos\theta_4}\cos\theta_4 & 0 \\ \frac{-e^{\gamma_3 d_3 \cos\theta_3}}{\eta_3} & \frac{-e^{-\gamma_4 d_3 \cos\theta_4}}{\eta_4} & \frac{e^{\gamma_4 d_3 \cos\theta_4}}{\eta_4} & 0 \\ 0 & e^{-\gamma_4 d_4 \cos\theta_4}\cos\theta_4 & -e^{\gamma_4 d_4 \cos\theta_4}\cos\theta_4 & -e^{-\gamma_5 d_4 \cos\theta_5}\cos\theta_5 \\ 0 & \frac{e^{-\gamma_4 d_4 \cos\theta_4}}{\eta_4} & \frac{-e^{-\gamma_4 d_4 \cos\theta_4}}{\eta_4} & \frac{-e^{-\gamma_5 d_4 \cos\theta_5}}{\eta_5} \end{bmatrix}$$

(4.9)

where $d_{1,2,3,4}$ are the consecutive positions of bone to muscle, muscle to fat, fat to skin, skin to air layers interfaces considering the physical dimensions of the real human organ. The 1×8 electric field intensity matrix [E] is expressed as:

$$[\mathrm{E}] = [\, E_{b1} \;\; E_{f2} \;\; E_{b2} \;\; E_{f3} \;\; E_{b3} \;\; E_{f4} \;\; E_{b4} \;\; E_{f5}\,]^{\mathrm{T}} \tag{4.10}$$

And $[\mathrm{b}] = [-E_{f1} e^{-\gamma_1 d_1 \cos\theta_1} \cos\theta_1 \;\; \frac{-E_{f1} e^{-\gamma_1 d_1 \cos\theta_1}}{\eta_1} \;\; 0 \;\; 0 \;\; 0 \;\; 0 \;\; 0 \;\; 0]^{\mathrm{T}}$ (4.11)

Now the reflection coefficient Γ and transmission coefficient T at each boundary are defined as the ratio of the amplitude of reflected and transmitted wave to the incident wave respectively and can be calculated at the i_{th} boundary by:

$$\Gamma_i = \frac{E_{bi}}{E_{fi}} \, e^{2\gamma_i d_i \cos\theta_i} \tag{4.12}$$

$$T_i = \frac{E_{f_{i+1}}}{E_{f_i}} \tag{4.13}$$

The dissipated power per unit volume in the i_{th} layer is

$$p_i = \frac{|E_i|^2 \sigma_i}{2} \tag{4.14}$$

The average power intensity per unit area along the layers in the i_{th} layer is given by:

$$\bar{S}_{av_i} = \frac{1}{2}\, Real(\bar{E}_i \times \bar{H}^*{}_i) \tag{4.15}$$

Another important characteristic is the specific absorption rate SAR which is the power dissipated per unit mass of the medium

$$SAR_i = \frac{|E_i|^2 \sigma_i}{2\rho_i} \tag{4.16}$$

Where ρ_i is the tissue density expressed in kg/m^3

A MATLAB code is written and used to calculate the values of α, β, γ ,η, SAR, S_{av}, electric and magnetic field intensity values in different tissue layers for the range of frequencies from 100 MHz to 10 GHz.

4.7 Verification and results of the model

Two cases are considered to verify the results, when the transmission starts from muscle in the 3 layers model and when the bone layer exist in case of 4 layers model. We compare the boundaries reflection coefficients in case of normal incident angle at frequencies 402 MHz, 900 MHz, 2.45 GHz, and 6 GHz with the results of [43]. The conductivity σ (S/m) and relative permittivity $\in_r$ of human tissues at these frequencies are shown in Table 6 [35].

The results obtained by this study show good agreement with that of [43] as illustrated in Tables 7 and 8 when the transmission starts from muscle tissue, and when it starts from bone respectively. The models consist of bone (20 mm), muscle (27.5 mm), fat (8.5 mm) and skin (1.5 mm).

Table 6. Dielectric parameters of human tissues

Frequency	Parameter	Blood	Bone	Muscle	Fat	Skin
402 MHz	$\in_r$	64.2	13.2	57.1	5.58	46.7
	σ	1.35	0.0915	0.797	0.041	0.689
900 MHz	$\in_r$	61.4	12.5	55	5.46	41.4
	σ	1.54	0.143	0.943	0.051	0.867
2.4 GHz	$\in_r$	58.3	11.4	52.8	5.29	38.1
	σ	2.5	0.385	1.71	0.102	1.44
6 GHz	$\in_r$	52.2	9.59	48.2	4.94	34.9
	σ	6.8	1.2	5.2	0.306	3.89
10 GHz	$\in_r$	45.1	8.12	42.08	4.6	31.3
	σ	13.1	2.14	10.6	0.585	8.01

Table 7. Comparative results of boundaries reflection coefficients of this study with [40] in case of transmission through muscle, fat, skin, to air

Boundary		402 MHz	900 MHz	2.45 GHz	6 GHz
Muscle to Fat	**Γ**	0.717	0.559	0.523	0.739
	Γ[43]	0.716	0.559	0.524	0.739
Fat to skin	**Γ**	0.364	0.396	0.588	0.738
	Γ[43]	0.364	0.396	0.588	0.738
Skin to Air	**Γ**	0.734	0.745	0.728	0.720
	Γ[43]	0.733	0.745	0.728	0.720

Table 8. Comparative results of boundaries reflection coefficients of this study with [40] in case of transmission through bone, muscle, fat, skin, to air.

Boundary		402 MHz	900 MHz	2.45 GHz	6 GHz
Bone to Muscle	**Γ**	0.568	0.439	0.348	0.380
	Γ[43]	0.567	0.439	0.346	0.380
Muscle to Fat	**Γ**	0.717	0.559	0.523	0.739
	Γ[43]	0.716	0.559	0.524	0.739
Fat to skin	**Γ**	0.364	0.396	0.588	0.738
	Γ[43]	0.364	0.396	0.588	0.738
Skin to Air	**Γ**	0.774	0.745	0.728	0.720
	Γ[43]	0.773	0.745	0.728	0.720

4.7.1 Reflection coefficient

Figure 15 shows the variation of reflection coefficient at the tissue interfaces for normal (0°) and oblique (5°, 9°, 13.5°) in-to-out angles of incidence with frequency when the transmission starts from the bone layer. The trend at the skin to air interface is almost steady in the whole range of frequencies at different incident angles. The reflection coefficients at the bone to muscle and muscle to fat interfaces show band pass shapes with one center frequency at 700 MHz for bone to muscle interface and two center frequencies at about 1.8 GHz and 8 GHz for muscle to fat interface.

At the beginning of the studied frequency range, the value of muscle to fat interface reflection coefficient is higher than that of the skin to air boundary. Both values increase with increasing frequency but with different rates until they become equal at around 160 MHz, then the reflection coefficient at skin to air starts to increase with higher rate before reaching steady value for frequencies greater than 200 MHz.

In contrast, the fat to skin interface shows a trend of low pass filter as the reflection coefficient is lower than 0.5 in case of normal incident wave and decreases with increasing the angle of incidence in the first mid band, while it rises gradually till reaching 0.7 at 7 GHz. It should be mentioned that we select the angle 13.5° as the upper bound because it is the maximum angle that can provide transmission out of the body at the whole studied frequency range. This angle is slightly less than the maximum incident angle at 100 MHz which is the lowest value in the stated frequency range.

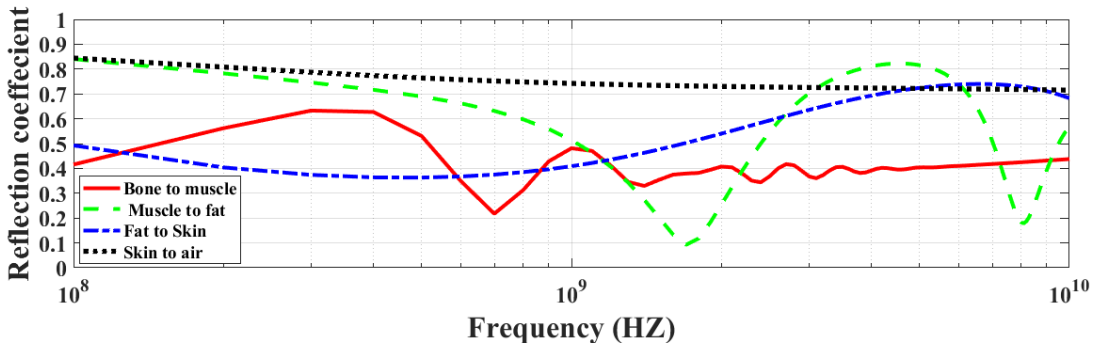

(a) 0° incident angle.

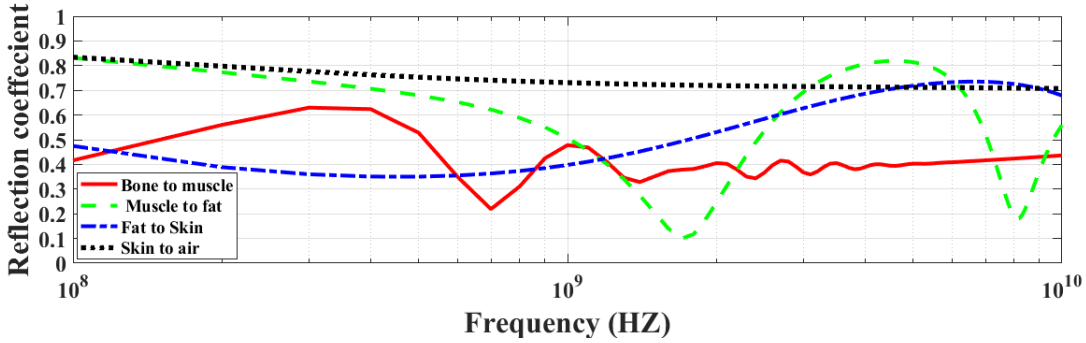

(b) 5° incident angle

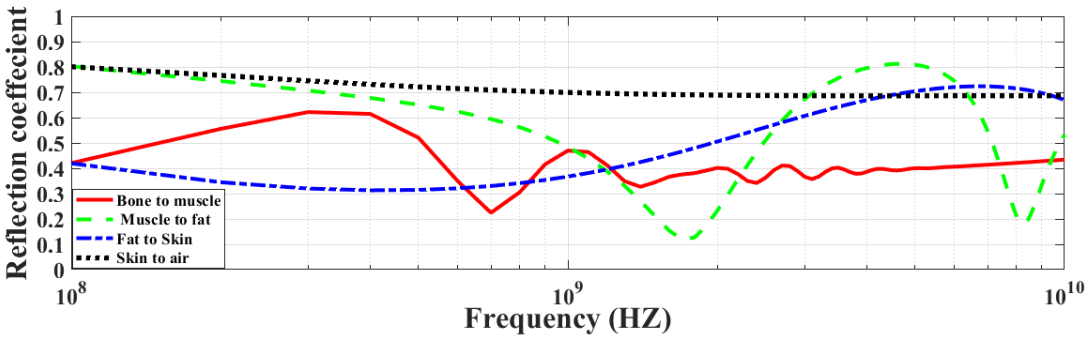

(c) 9° incident angle

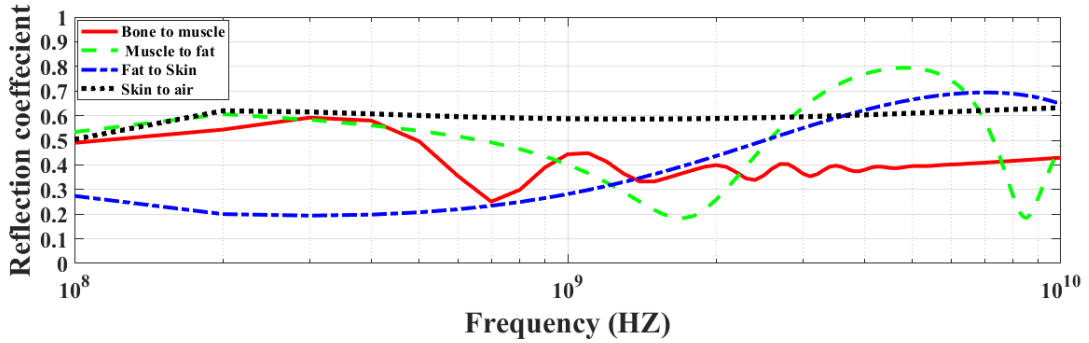

(d) 13.5° incident angle

Figure 15. Variation of reflection coefficient with frequency at incident angles: (a) 0°, (b) 5° , (c) 9° , (d) 13.5° for four layers model

The variation of reflection coefficient with the frequency when the propagation starts from the muscle layer is illustrated in Figure 16 in cases of 0°, 2°, 4°, 5.5° angles of incidence. The maximum incident angle is selected to be 5.5° as it can achieve transmission out of the body at the whole range of frequencies. This value is slightly less than the maximum angle of incidence on the muscle to fat boundary at the lowest frequency in the studied range. If the angle of incidence is higher than the maximum selected angle, we have to exclude some lower frequencies from the studied band at which the EM wave will be completely reflected and no wave will be received outside the body. The skin to air reflection coefficient is almost steady for normal and oblique incident angles at the whole investigated range of frequencies. It also shows the highest value while the fat to skin interface records the lowest reflection coefficient

in the first half of frequency range. Frequencies higher than 1GHz experience a kind of fluctuation in the reflection coefficient values between the three interfaces. The muscle to fat interface shows two minima at frequencies about 1.8 GHz and 8 GHz. In general, the reflection coefficients at the three interfaces for 5.5° incident angle experience lower values compared to the corresponding values at other incident angles.

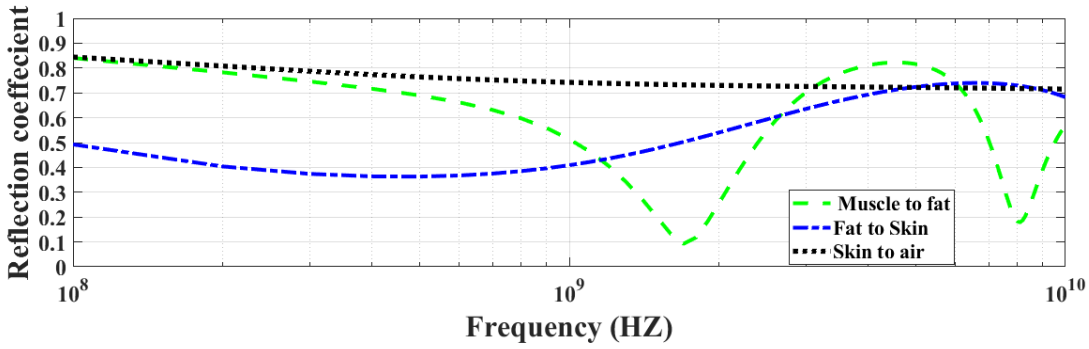

(a) 0° incident angle

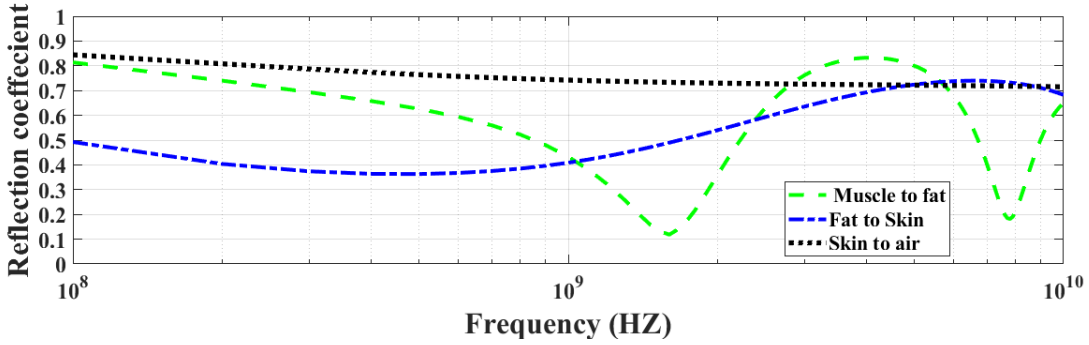

(b) 2° incident angle

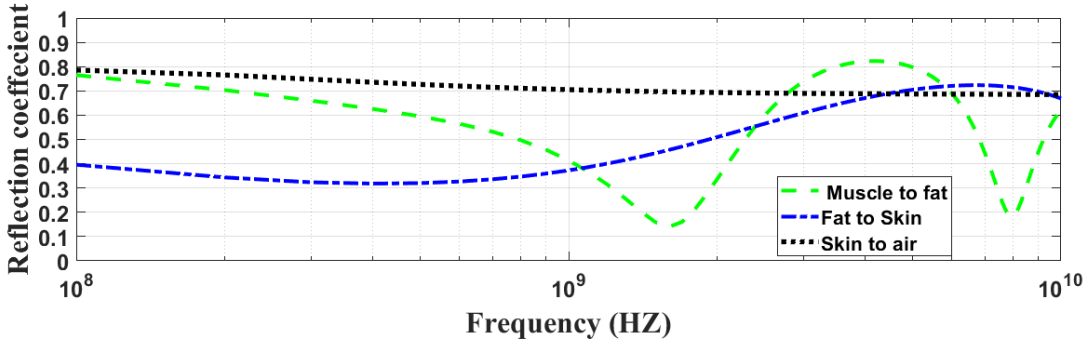

(c) 4° incident angle

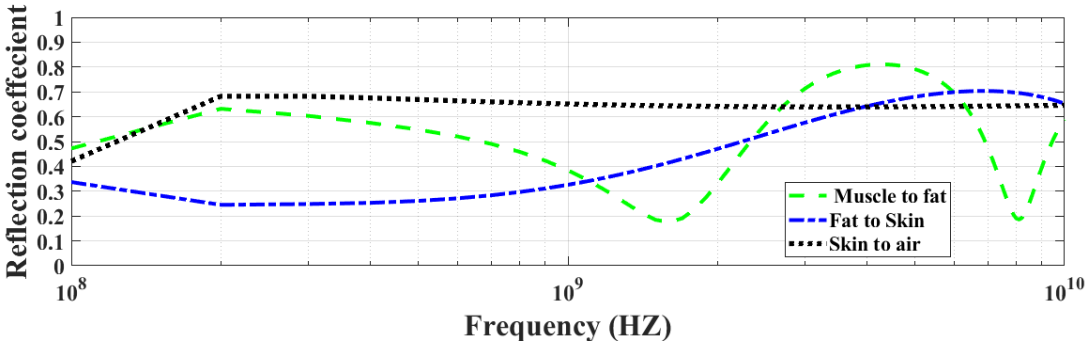

(d) 5.5° incident angle

Figure 16. Variation of reflection coefficient with frequency at incident angles: (a) 0° , (b) 2° , (c) 4°, (d) 5.5° for three layers model

4.7.2 Effect of multiple reflection

Part of the main incident EM wave on the first bone-muscle interface is reflected in the bone layer. The first reflected wave propagates toward the left muscle-bone interface with the same incident angle of the main wave. The reflection process is repeated along the bone layer. If the incident angle of the main wave is smaller than the maximum incident angle that can produce transmission out of the body as in Table 6, the reflection from the left muscle-bone interface will also produce output transmission. Figure 17 shows the effect of the multiple reflections at the bone layer on the output transmission. At a constant distance from the skin to air border, the main transmission is received at height l_{rad} while the transmission due to the multiple

reflection levels at the bone layer is received at $l_{rad} + b, l_{rad} + 2b, l_{rad} + 3b, etc.$ The same process occurs in the muscle, fat and skin tissue layers.

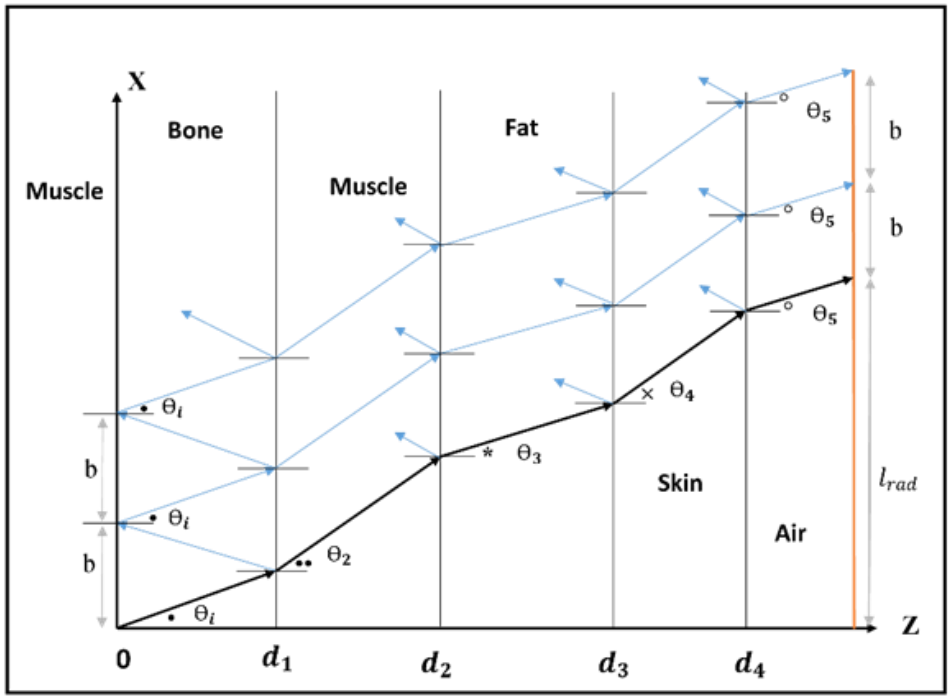

Figure 17. Effect of multiple reflection

Table 9. Effect of multiple reflection levels at the bone on the transmitted average power density.

Tissue	1st level W/m^2	2nd level W/m^2	3rd level W/m^2	4th level W/m^2
Bone	$4.7\text{x}10^{-6}$	$4.069\text{x}10^{-8}$	$3.678\text{x}10^{-10}$	$3.204\text{x}10^{-10}$

Table 9 illustrates the results of the average power density transmitted out of the body and produced by the multiple reflection at the bone layer for oblique incident EM wave with 10° incident angle and main transmission of $5.399\text{x}10^{-4}$ W/m^2 at a constant distance from the model.

4.7.3 Average power density

Figure 18 represents the time average pointing vector S_{av} at any point in the wave propagation direction at operating frequencies 400 MHz, 900 MHz, 2.4 GHz, 6 GHz, 10 GHz and 10° incident angle when the wave is travelling through the 4 layers model to air. We can find that the value of S_{av} decreases with increasing frequency as the EM wave penetration through the human tissue decreases with frequency.

The frequency, the strength of EM wave and the composition of the tissue in the body (water, fat, and salt content) play a key role concerning the amount of energy which is absorbed in body tissues from the EM field by heat conversion. The higher the frequency of the EM field the stronger the absorption at the body tissue, therefore the higher the frequency the shorter the distance the field can penetrate into the body. However, the depth of penetration is proportional to the initial field strength. The absolute depth of penetration is generally larger when the initial field strength is high compared to a low initial field strength. The current results are corresponding to initial electric field of 1 V/m.

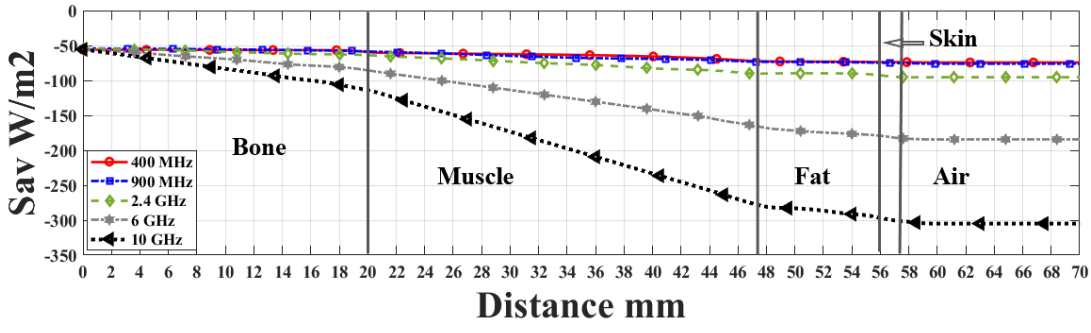

Figure 18. Variation of average power density along the four layers model at different frequencies

The dielectric properties of the tissue, as permittivity and conductivity, are governed by the tissue composition and distribution of water molecules, ions and other molecules. This influences the level of absorption of the field in different tissues. A higher conductivity due to a higher water or salt content, increases the interaction of the field with the tissue and thus the thermal effect. Hence, there are areas in the body with higher local heating and areas with lower heating compared to the surrounding tissues. Bone and fat tissues, for example, are heated less than other tissues because of their low conductivity due to low water content. The depth of penetration is associated with the tissue-depending thermal effect. It is higher in fat and bone tissues than in muscle tissue, as muscle tissue absorbs the field to a greater extent and thus the field energy is converted into heat most efficiently.

The variation of S_{av} with the distance in case of three layers model when the implanted device is in the muscle and the wave propagates through the model to outside the body with a 4° incident angle is shown in Figure 19.

Beside the decrease in S_{av} as the operating frequency increase, we find that the value of S_{av} at the last layer before the EM wave emerge to air is higher than the value when transmission starts from bone for the whole frequency range as the EM wave penetration into the tissues is higher.

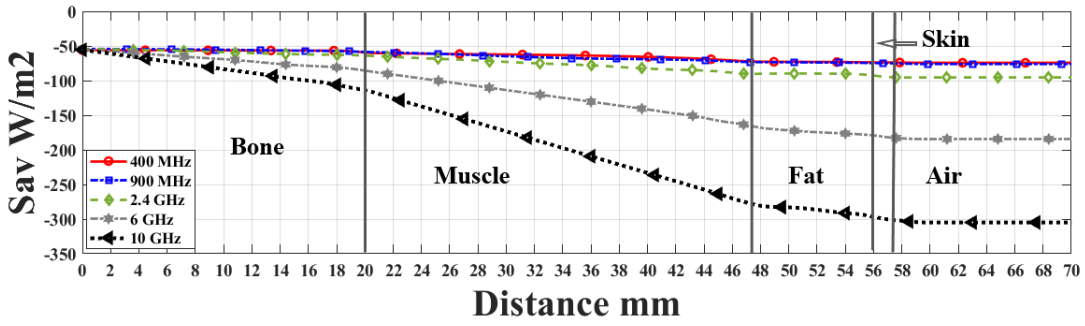

Figure 19. Variation of average power density along the three layers model at different frequencies

4.7.4 Specific absorption rate SAR

For a tissue density ρ_i (Kg/m^3), conductivity σ_i and dissipated power density P_i (W/m^3), the average local SAR (W/kg) at position (i) is given by:

$$SAR = \frac{P_i}{\rho_i} = \frac{|E_i|^2\,\sigma_i}{2\,\rho_i} \text{ W/kg} \tag{4.17}$$

The variation of SAR along the different tissues of a model of human humerus at 400MHz, 6 GHz, and 10 GHz is shown in Figure 20. At the beginning of the tissue, the value of SAR is high at the higher frequencies due to the electric field absorption and heat conversion. The following layers experience a low value of SAR at higher frequencies because most of the EM wave is already absorbed. As the penetration of the 400 MHz wave through the tissue is higher than the other frequencies, it shows a clear behavior of SAR along the tissue. The curve shows a low value of SAR at bone and fat tissue than at muscle and skin due to the difference in electrical properties and composition of the tissue. This SAR values give advantage for the lower frequencies over the other studied frequencies. The different densities of human upper arm tissues are given in table 3.

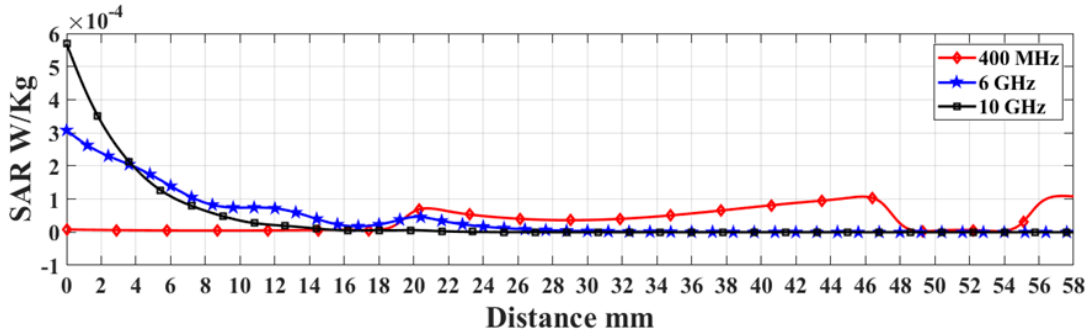

Figure 20. Variation of specific absorption rate along the three layers model at different frequencies

4.7.5 Average monitoring power density

The average monitoring power density (AMPD) is defined as the difference between the average power densities of fractured and normal bone. This difference in average power densities is used for monitoring the bone healing. As an example, a 45° oblique fractured bone is considered. The range from 31° to 45° of incident angles is used in order to guarantee a transmission of EM wave outside the body. The corresponding observation angles for these incident angles can be calculated by (2.25) at any distance from the skin.

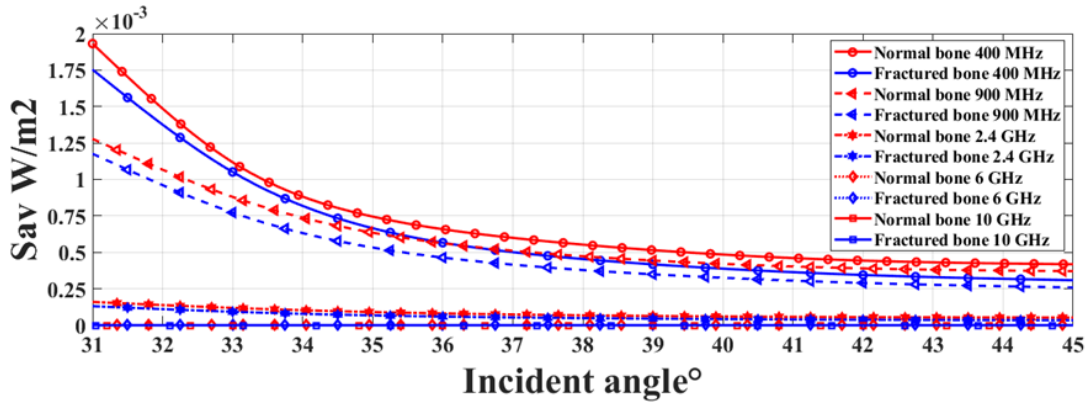

Figure 21. Comparison between average power densities with incident angle in cases of normal and fractured bones at different frequencies

A comparison between the average power density S_{av} for the normal and oblique fractured bone at the studied frequencies and at distance 50 cm from the skin to air interface is shown in Figure 21.

Figure 22 gives information about the variation of the AMPD with 31° to 45° incident angles on the fracture layer which help the designer finding the best angle of observation outside the body as illustrated in section (2.4).

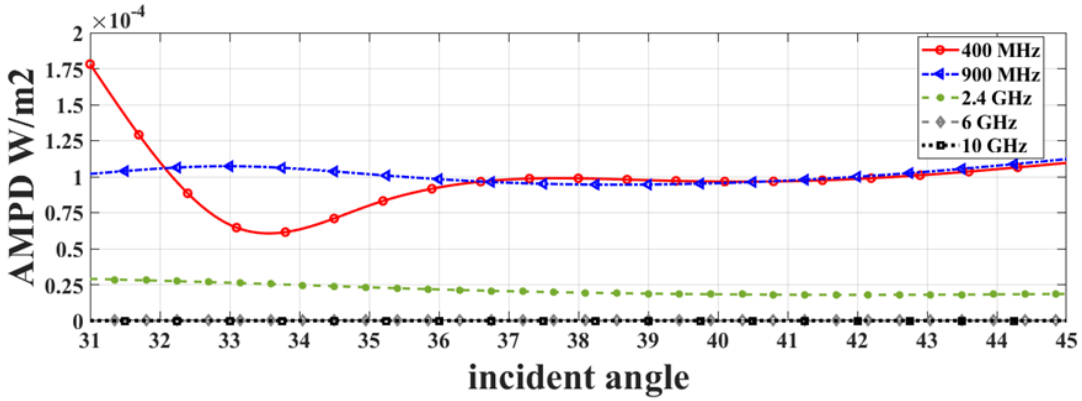

Figure 22. Variation of average monitoring power density with incident angle at different frequencies

At 400 MHz the AMPD shows a peak value at 31° and decreases with increasing the incident angle till it dips to minimum at 33.5°. The trend starts to increase and becomes almost steady for incident angles greater than 37°.

The value of AMPD in case of 900 MHz is comparable to that of 400 MHz for incident angles greater than 36°. Due to the attenuation of the electric field in the human tissues at the high frequencies, there is a remarkable reduction in the average power density and the AMPD at 2.4 GHz, 6 GHz, and 10 GHz. The value of the AMPD at 400 MHz and 900 MHz are higher than that of other frequencies which result in better monitoring. The lower frequencies are selected for the bone fracture monitoring as

they are easier in practical implementation, and due to the ability of size miniaturization of the implanted antenna when there is a need of miniaturization.

Chapter 5

SIMULATION AND VERIFICATION

In this chapter, planar and cylindrical tissue models are considered for simulation. The tissues dimensions are defined considering the physical dimensions of human femur. Due to the low cost, design simplicity and ease of fabrication on PCB, the half wave dipole antenna is selected to test this application. Two different half wave dipole antennas are designed and used for monitoring the fracture healing in cylindrical model, which are planar and meandered antenna. The antennas are fully insulated by biocompatible silicon film, and a Roger 3010 material is used as substrate.

5.1 Planar tissue model

The first simulated model is a planar multi-layered model that is composed of a consecutive bone, muscle, fat, and skin tissue as shown in Figure 14(a). The simulation is done by the CST microwave studio. The antenna in Figure 24 (b) is implanted at the surface of the bone and the EM wave propagates along the bone, muscle, fat, skin layers to air.

Figure 23 experiences the variation of the simulated average far field power density at distance 50 cm from the skin surface for normal bone and oblique fractured bone.

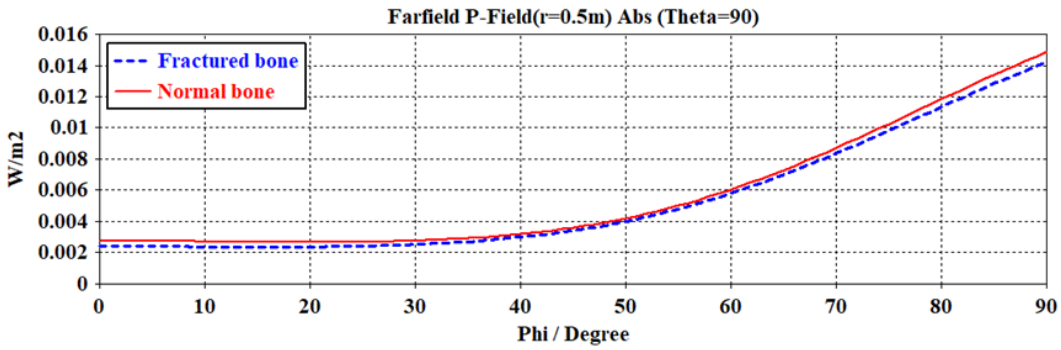

Figure 23. Variation of average power density along the planar tissue model at 900 MHz

The pattern of average power density shows a similar trend compared to the results in Figure 21. The angles in Figure 21 are the incident angles on the bone layer, while in Figure 23, the angles are the observation angles in the air layer outside the body, as the 45° incident angle produces 0° observation angle following equation (2.25). Considering the x-z plane of Figure 14, the result of simulation shows agreement with the analysis as the output transmission increases from minimum to maximum when the observation angle increases from 0° to 90°. As the radiation pattern of half wave dipole antenna is almost isotropic, the output transmission can be at observation angles up to 90°. In case of narrow beam antenna with an angle lower than the maximum incident angle in Tables 1-3 for the normal and fractured bone cases respectively, the maximum output transmission will be lower than 90°. Table 10 shows the variation of the angle θ_{obs} as in Figure 3 with respect to the incident angle at distance 50 cm from the skin, at 900 MHz.

Table 10. Variation of observation angle with incident angle at 900 MHz

$\boldsymbol{\theta_{in}}$	**45°**	**43°**	**41°**	**39°**	**37°**	**35°**	**33°**	**31°**	**29°**
$\boldsymbol{\theta_{obs}}$	0°	7.1°	14.4°	21.8°	29.6°	38.1°	47.6°	59.2°	78.2°

5.2 Monitoring of femoral shaft fracture healing

5.2.1 Cylindrical tissue model

The second proposed model in this study is a cylindrical tissue model shown in Figure 24 (a) as an approximation to the real human femur. This model is composed of concentric bone, muscle, fat, skin cylindrical layers. A half wave dipole antenna is implanted between the bone and muscle tissues.

In this simulation the implanted antenna is parallel to the z axis and the cylindrical tissue layers are perpendicular to the x-y plane. The cylindrical model is concentric with the z-axis. The oblique fracture is an elliptical cylindrical layer that makes 45° rotation around the y axis, while the transverse fracture is represented by circular disc perpendicular to the z-axis as shown in Figure 24(c), (d) respectively. The dimensions of the model are designed considering the physical human femur dimensions which are presented in Table 11.

Table 11. Dimensions of tissue model

Tissue and implanted antenna	**Dimensions in mm**
Bone	27.2
Muscle	45
Fat	10.4
Skin	1.9
Fracture thickness	2

We compare the far field average power densities at three constant θ angles 30°, 60°, 90°. For each value of θ we record the corresponding observation angle at which the maximum AMPD is achieved. The observation angle in this simulation is the ϕ angle

measured from the x-z plane to the y-z plane. We select the position of the implant at 90° at which the S parameter difference between the normal and both types of fractured bone is of maximum value.

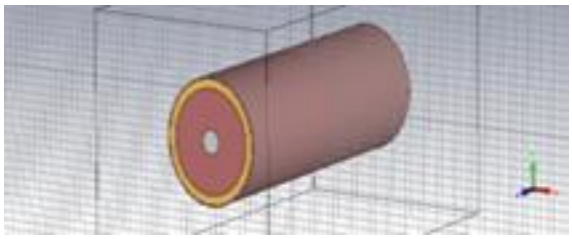

(a)

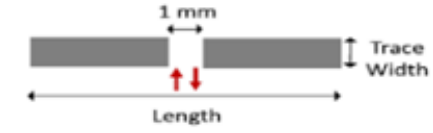

(b)

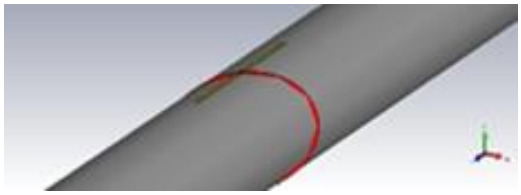

(c)

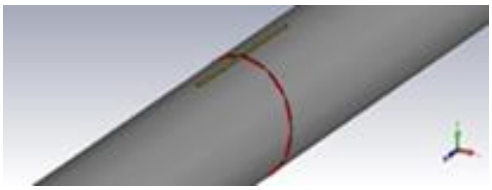

(d)

Figure 24. (a) CST cylindrical tissue model, (b) Half wave dipole antenna, (c) Oblique fractured bone, (d) Transverse fractured bone.

Taking into account the biocompatibility with the human tissues, the antennas are fully insulated by an ultrathin film of silicon and a substrate of Rogers R03010. The substrate material has a thickness h = 0.638 mm, relative permittivity ϵ_r=10.2, and loss tangent is tan δ = 0.0022.

5.2.2 Planar antenna

The normal and fractured bone models are simulated first by using a planar half wave dipole antenna. The wavelength at 900 MHz in muscle is 44.92 mm and in bone is 94.22 mm. we start the simulation by antenna length of half wave length in bone and tune it by trial and error to resonate at the operating frequency which is achieved at 41 mm. The antenna is shown in Figure 25 and Table 12 illustrates its dimensions.

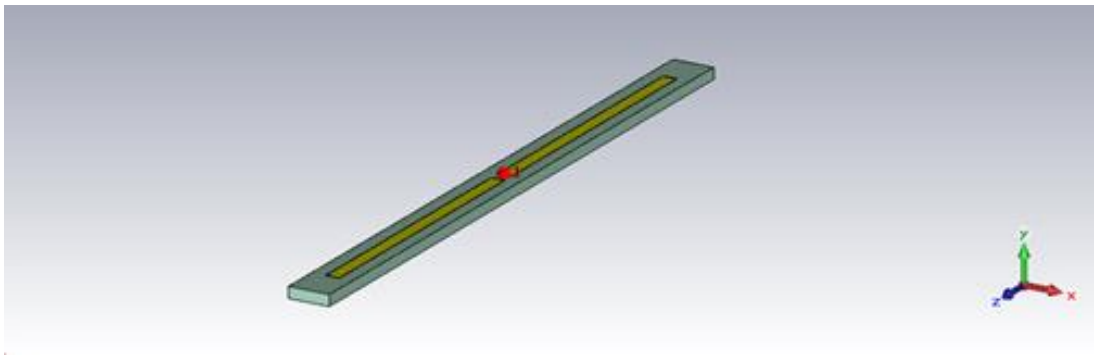

Figure 25. Planar antenna

Table 12. Dimensions of planar half wave dipole

Parameter	Dimension in mm
Length	41
Trace width	1
Gab	1
Substrate length	46
Substrate width	5
Substrate thickness	0.638

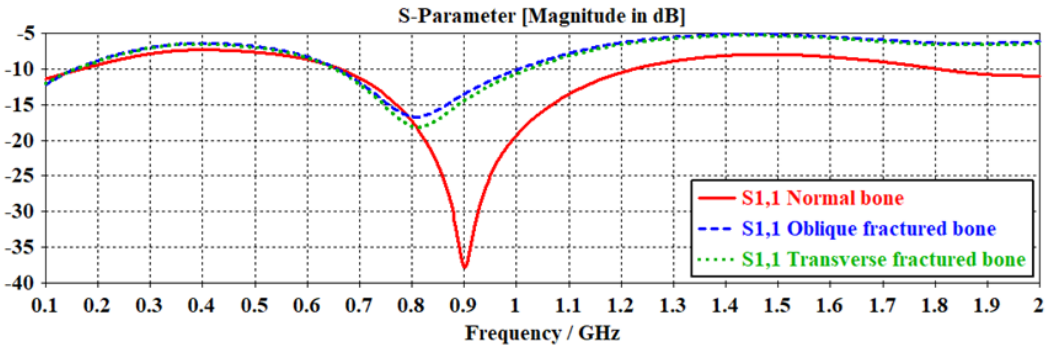

Figure 26. S parameter comparison between normal, oblique fractured, transverse fractured bone measured at φ =90° using insulated planar half wave dipole antenna.

Figure 26 shows a difference of 24.2 dB in return loss between the normal and oblique fractured bone case and of 23.3 dB between the normal and transverse fractured case.

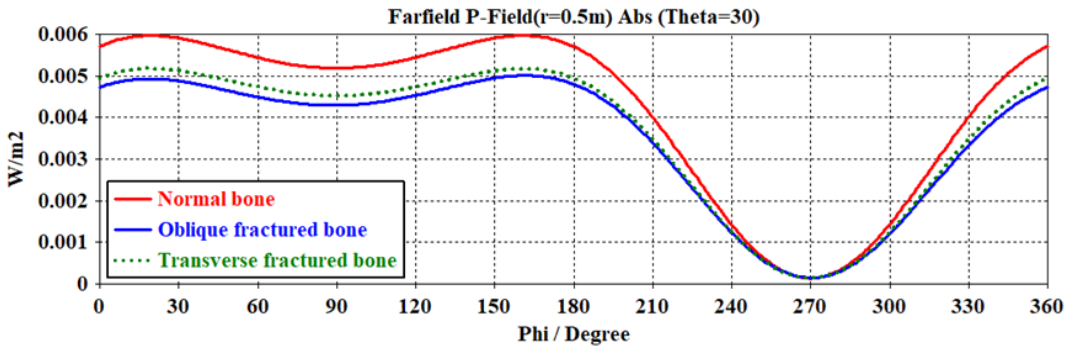

Figure 27. Variation of average power density for normal, oblique fractured and transverse fractured bone measured at constant value of Θ = 30° at 900 MHz by insulated planar half wave dipole antenna

The variation of transmitted average power densities with angle of observation ϕ is shown in Figure 27 for the constant value 30° of angle θ and default excitation signal of CST. The maximum difference between the normal and fractured bone average power densities occurred at θ =30° and two different observation angles 18°, 162°. Table 13 illustrates the transmitted average power density in case of normal bone, the AMPD for the fractured bone cases, and the percentage reduction in transmission due to the fracture.

Table 13. Comparison between AMPD of transverse, and oblique fractured bone by planar half wave dipole antenna at 900MHz

θ	**Observation angle**	**Transmitted average power density normal bone (μW/m$^{2)}$**	**AMPD of transverse fractured bone (μW/m^2)**	**AMPD of oblique fractured bone (μW/m^2)**
30°	18°, 162°	5970	792	1039
			13.27% Reduction	17.4% Reduction
60°	190°, 350°	3806	466	646
			12.23% Reduction	16.97% Reduction
90°	270°	4494	548	547
			12.19% Reduction	12.17% reduction

Monitoring by planar half wave dipole antenna shows 17.4%, 13.27% reduction in the transmitted average power density for the oblique and transverse fractured bone respectively at the observation point.

When the bone is fractured, there is a bleeding into the area that leads to inflammation and blood clotting. The healing process starts by replacing the clotted blood with fibrous tissue and soft callus starting from both sides of the fracture. The healing continues and the soft callus is replaced by hard bone in several weeks. In the last phase of bone healing, bone continues to form and becomes compact, returning to its normal shape in some months. Figure 28 shows the fracture levels at (2, 1, 0.5, 0.25) mm recorded at the point of observation, as the bone grows during the healing process.

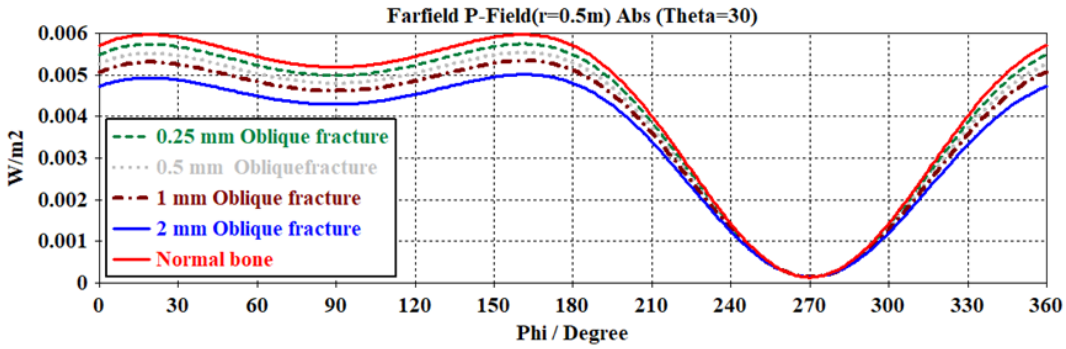

Figure 28. Variation of average power density for normal and oblique fractured bone measured at constant value of Θ = 30° for (2, 1, 0.5, 0.25) mm fracture

5.2.3 Meander antenna

To miniaturize the size of the implanted antenna in human body we present a meander half wave dipole antenna shown in Figure 29. By this miniaturization, the effective length of the radiator part of the antenna is reduced to 27 mm which is 65.85% of the linear half wave dipole at 900 MHz and the effective width increases to 5.42 mm. The overall length of the antenna is reduced by 22.9%. The segment length is selected

from some trials to facilitate the placement of the antenna within the femor model and achieving accepted results. Table 14 expresses the dimensions of the antenna.

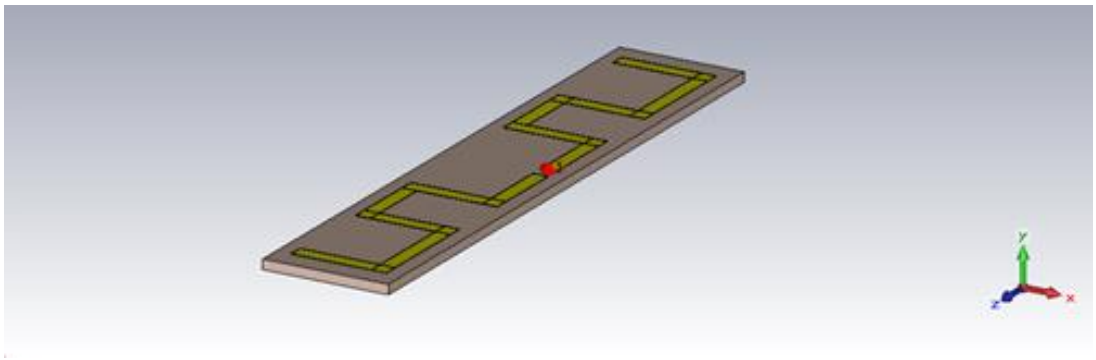

Figure 29. Meander antenna

Table 14. Dimensions of meandered half wave dipole

Parameter	Dimension in mm
Segment length	6.25
Trace width	1
Gap	1
Substrate length	35.5
Substrate width	8.25
Substrate thickness	0.638

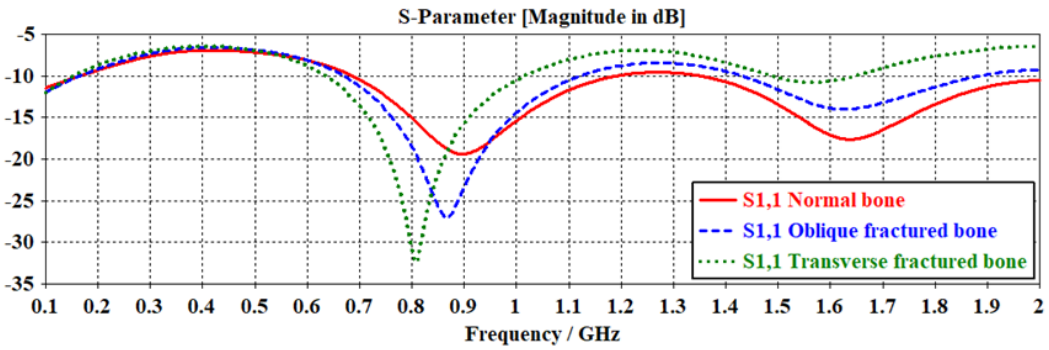

Figure 30. S parameter comparison between normal, oblique fractured and transverse fractured bone measured at 90° by using meander half wave dipole antenna.

The S parameter curves of normal bone and the two types of fractured bone when using the meandered antenna are shown in Figure 30. A 3.7 dB difference between the normal bone and transverse fractured bone is recorded while the difference between the normal and oblique fracture bone cases is 4 dB.

The variation of transmitted average power density with observation angle for the 30° value of θ is illustrated in Figure 31 when using the meandered half wave dipole antenna. The maximum value of difference in average power densities is recorded at 30° of θ like the cases of planar and cylindrical half wave dipole.

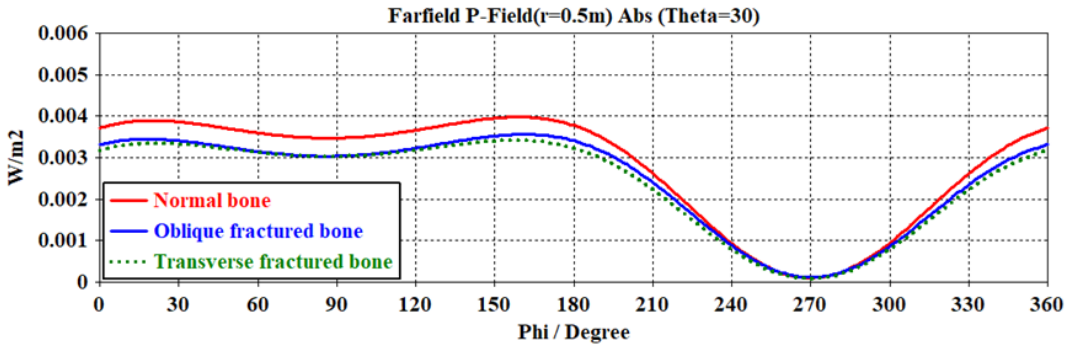

Figure 31. Variation of average power density for normal, oblique fractured and transverse fractured bone measured at constant value of Θ =30° at 900 MHz by using insulated meander half wave dipole antenna..

Table 15. Comparison between AMPD of transverse, and oblique fractured bone by meandered half wave dipole antenna at 900MHz

θ	**Observation angle**	**Transmitted average power density Normal bone ($\mu W/m^2$)**	**AMPD of transverse fractured bone ($\mu W/m^2$)**	**AMPD of oblique fractured bone ($\mu W/m^2$)**
30°	20°, 160°	3892	548	442
			14.1% Reduction	11.36% Reduction
60°	190°	2591	377	211
			14.6% Reduction	8.14% Reduction
90°	267°	2889	409	99
			14.16% Reduction	3.4% Reduction

Due to the low radiation efficiency of the meander antenna, the average power density is lower than the planar antenna in normal and fractured bone cases. The results show a reduction of 11.36% and 14.1% in the transmitted average power density for the oblique and transverse fractured bone respectively. The AMPD results are given in Table 15.

5.2.4 Experimental setup

In order to verify the validity of the new monitoring technique and simulation results, experimental measurements are carried out on a non-living animal model shown in Figure 17. An upper arm of a cow which is similar in composition to the human femur is selected as the experimental subject. The experimental equipment includes the selected model, half wave dipole antenna, vector network analyzer, SMA cables and connectors.

(a)

(b)

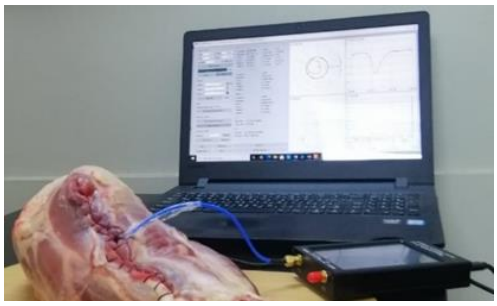

(c)

(d)

Figure 32. The experimental set-up (a) The normal bone model, (b) The fractured bone model, (c) The set, (d) Antenna and SMA cable.

In the first experiment, the half wave dipole wire antenna is implanted at the boundary between the bone and the muscle tissue of the normal bone model. The antenna is connected to port1 of the vector network analyser by an insulated SMA cable and then the return loss is measured for the normal bone case. In the second experiment, the bone shaft is broken obliquely and the return loss measurement is repeated. Figure 33 shows the experimental measurements of the return loss for the normal and fractured bone cases. It was difficult to break the bone while preserving the surrounding muscle

tissue unaffected. A specialist assisted in opening the tissue and returning it with surgical stutures as happens surgically in such cases.

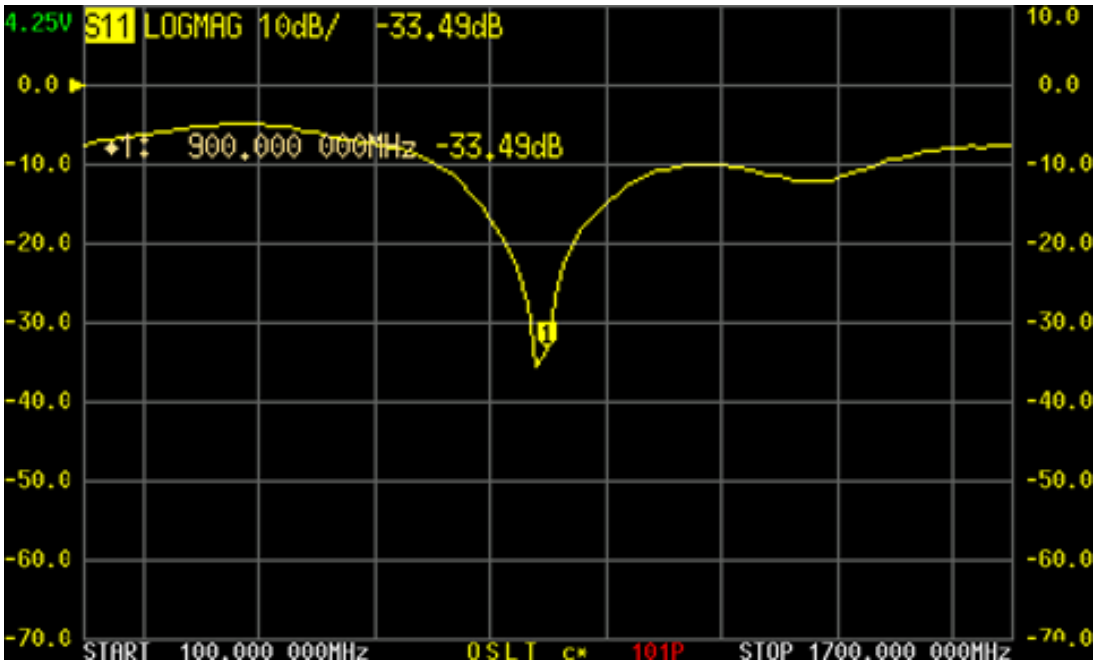

(a) Normal bone

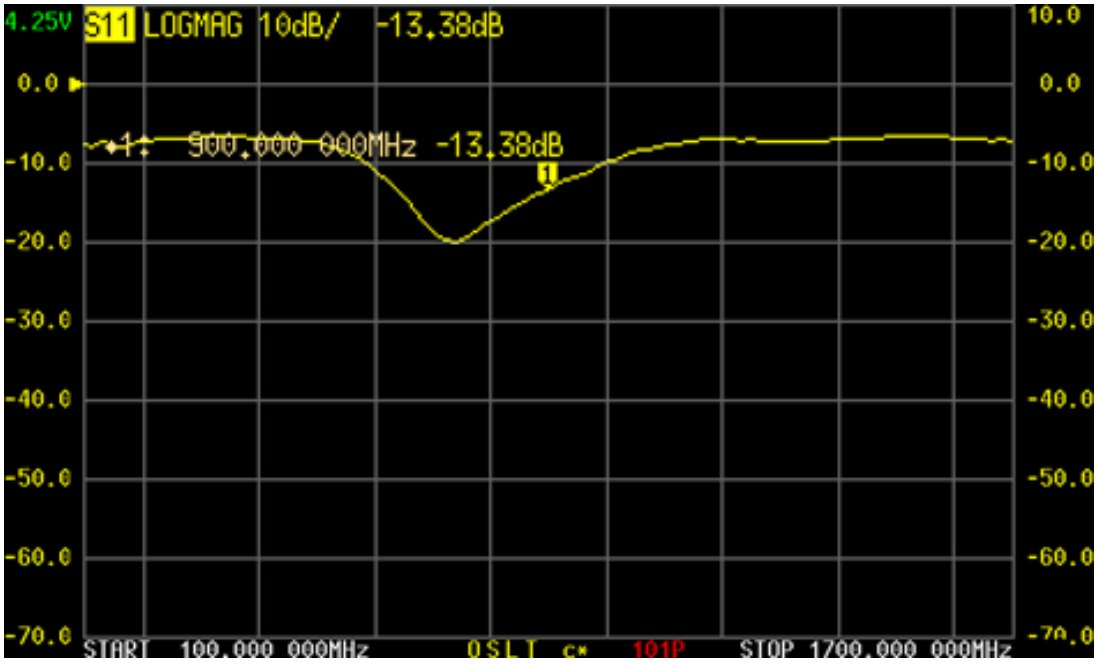

(b) Fractured bone

Figure 33. Measured S parameter in case of (a) Normal bone, (b) Fractured bone

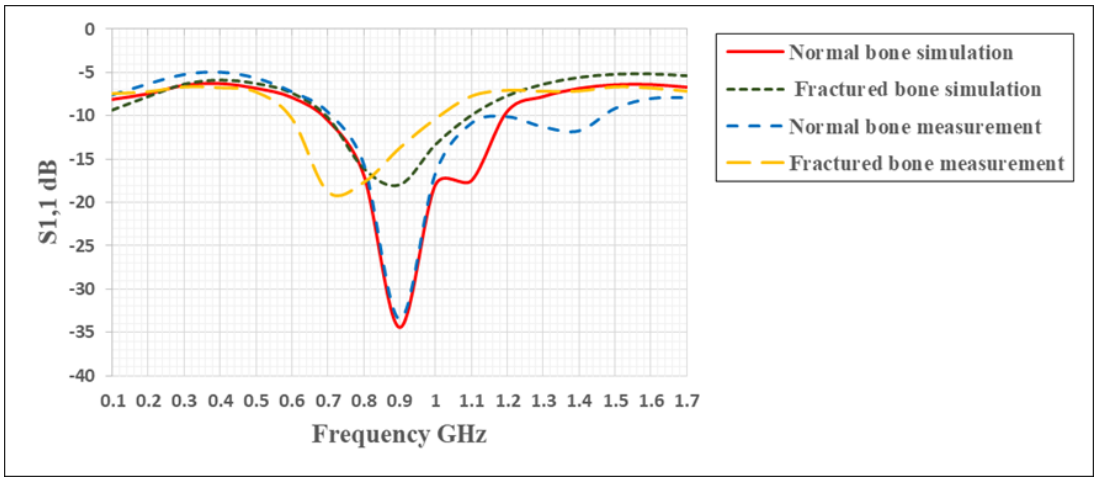

Figure 34. Measured and simulated S parameter of normal bone and fractured bone

The measurement results are reasonably in good agreement with the simulation as shown in Figure 34. We relate the little deviation between the simulation and measurements to the difference in properties between living and non-living tissues and to the thickness and angle of fracture, as it was not easy to break the bone with the same accurate angle as selected in simulation.

5.3 Monitoring of upper arm fracture healing

The human's upper arm (humerus) is the long bone that runs from the shoulder to the elbow. The humerus shaft fracture is one that localized in the mid portion of the upper arm as shown in Figure 35 (a). This fracture is a common injury and is always a consequence of a fall with an outstretched hand, or car accidents. The treatment can be with or without surgery according to the fracture pattern and associated injury. A temporarily splint extending from the shoulder to the forearm and holding the elbow bent at 90 degree can be used for initial management of the fracture.

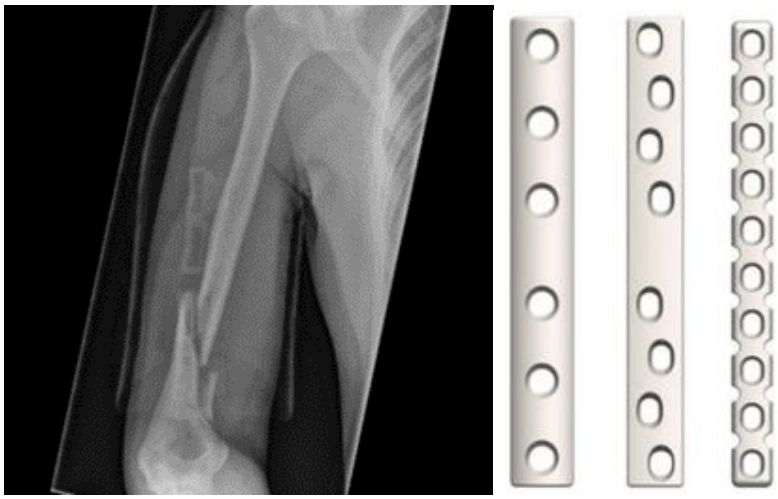

(a) (b)

Figure 35. (a) Upper arm fracture, (b) Fixation plates.

Non-operative treatment usually includes the placement of fracture bracing that will be replaced by a cylindrical brace (Sarmiento brace) three to four weeks later that fits the upper arm while leaving the elbow free. Surgery usually involves internal fixation of the fragments with plates shown in Figure 35 (b), screws or a nail [44].

The post-surgery follow up of the fracture is by X-Ray images, and the patient is monitored at the clinic by serial radiographs at 10 days, 3 weeks, 6 weeks and as needed thereafter. The proposed monitoring technique in this study saves the X-Ray exposure and visits to clinic by monitoring at homes. This technique is based on an implanted antenna within the humerus and recording the value of the transmitted power at the far field of it [45]. The human tissue is a lossy medium for electromagnetic wave and the fracture adds extra lossy tissues. The difference in transmitted power between the normal and the fracture cases monitors the healing status [29].

5.3.1 The upper arm model

An approximated cylindrical model of human upper arm proposed for the simulation of this monitoring technique is shown in Figure 36. The model is composed of concentric cylindrical layers of bone, muscle, fat, skin, and finally the splint layer which is used to hold the fractured bone in place during the healing period. A metallic fixation plate is used surgically to fix the fracture in place. The fracture is modelled by an additional layer in the bone. A circular disc layer perpendicular to the bone shaft represents the transverse fracture and an elliptical disc layer represents the oblique fractured humerus. Table 16 summarizes the dimensions of the model [46]. The normal and fractured humerus models are simulated by CST microwave studio at 402 MHz.

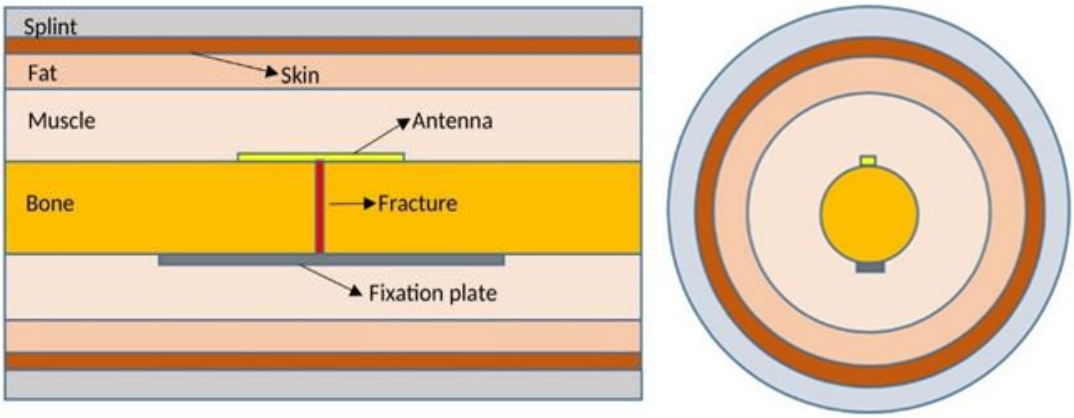

Figure 36. Cylindrical model of fractured humerus.

Table 16. Dimensions of the model and fixation plate

Tissue thickness	Dimension in mm
Bone	12.5
Muscle	27.5
Fat	8.5
Skin	1.5
Length of model	350
Fracture thickness	2
Splint thickness	3
Fixation plate length	100
Fixation plate width	8
Fixation plate thickness	3

5.3.2 Simulation and discussion

The described model is simulated by CST microwave studio. Due to the morphology of the human upper arm, there is a limited space for the implanted antenna. We select a half wave dipole antenna due to simplicity and suitability to be implanted in the cylindrical model. In half wave dipole antenna, the two conductors installed in line and a small gap is left between them. The voltage is attached to the center of both conductor via SMA connector. The length of the dipole ought to be half of the wavelength [47].

The antenna is implanted parallel to the bone axis at the border between the bone and the muscle tissue. The model is concentric with the z-axis while the transverse fracture is modelled by a circular disc layer perpendicular to it. The oblique fracture is represented by elliptical layer and makes 30°, 60° with the y-axis.

For biocompatibility with human tissue, the radiator part is coated by an ultrathin sheet of silicon and a substrate of FR-4 of ε_r =2.4 and loss tangent of 0.025 are used. Figure 37 shows a cross sectional elevation and plan of the antenna and the dimensions within human body are illustrated in Table 17.

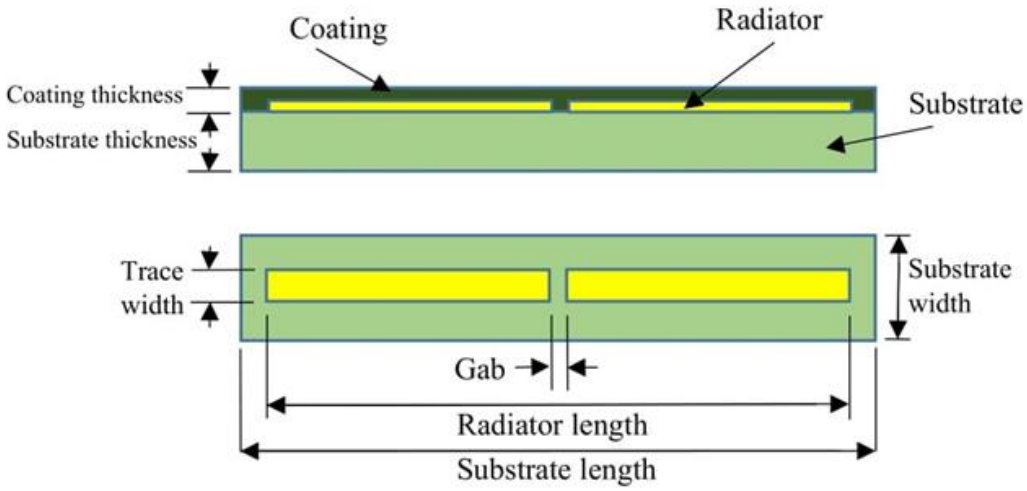

Figure 37. Insulated planar half wave dipole antenna.

When simulating the antenna in air, the wavelength is 745.75 mm and the first resonance of the dipole is expected to occur at 0.47 wavelength [47]. For a trace width of 1 mm the minimum return loss of -33.5 dB is obtained at length 350.5 mm. The power pattern of the antenna in air shows a symmetric pattern around the radiator as in Figure 38 (a), 38 (b).

According to the electrical properties of human tissues, the wavelength of frequency 402 MHz in muscle is 312.09 mm and in bone is 206.02 mm. As the antenna in the proposed technique is implanted at the bone to muscle interface, it resonates at length 111 mm and trace width 1 mm.

Table 17. Antenna dimensions within human tissue.

Antenna parameter	Dimension in mm	Antenna parameter	Dimension in mm
Radiator length	111	**Substrate length**	116
Radiator width	1	**Substrate width**	5
Radiator thickness	0.035	**Substrate thickness**	0.5
Gap	1	**Coating thickness**	0.01
Trace width	1		

The attenuation of the EM field within the tissues affects the symmetry far field power pattern of the antenna as shown in Figure 38 (c), 38 (d).

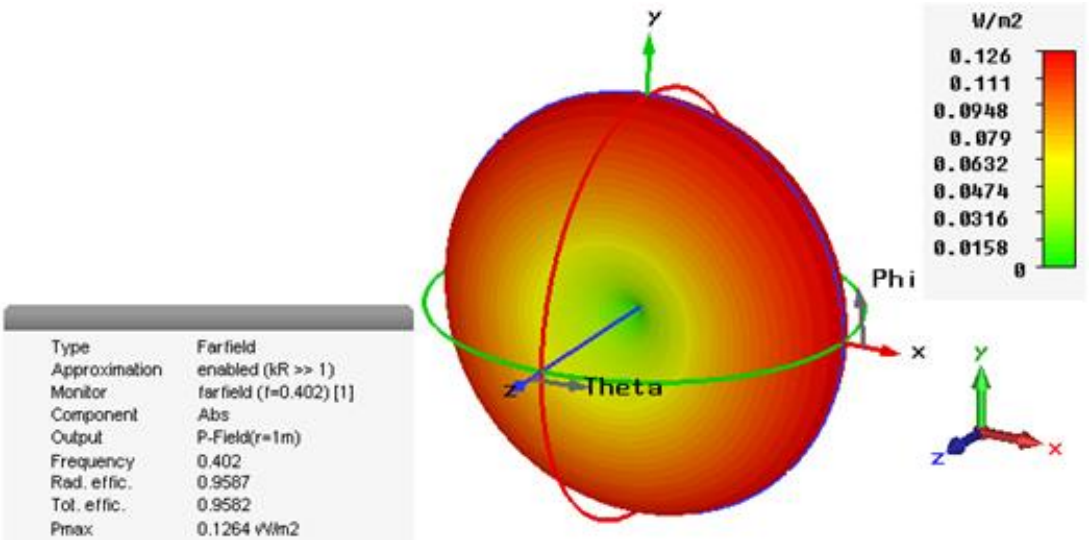

(a) 3D far field pattern of antenna in free space

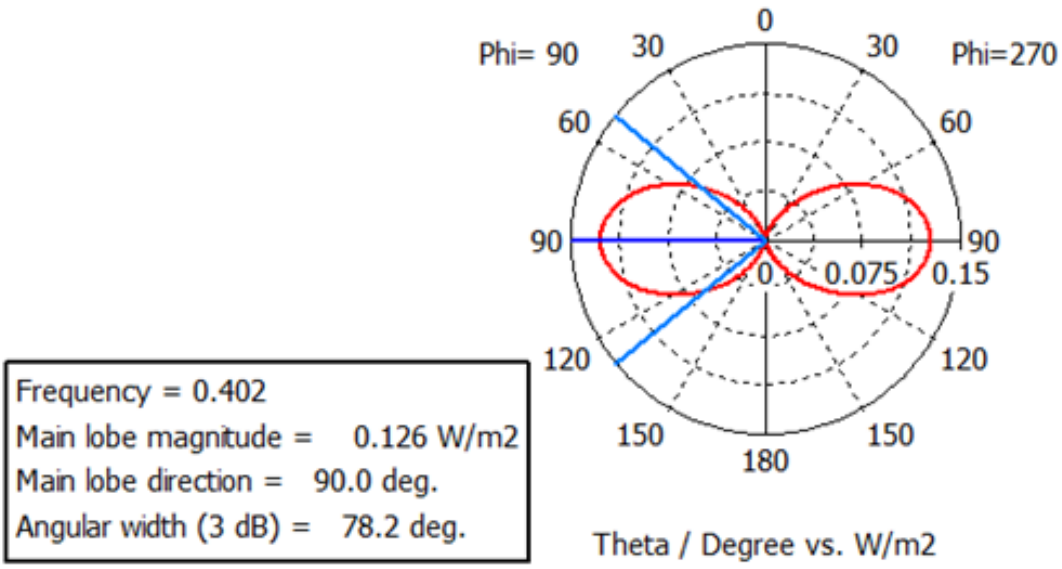

(b) 2D far field pattern of antenna in free space

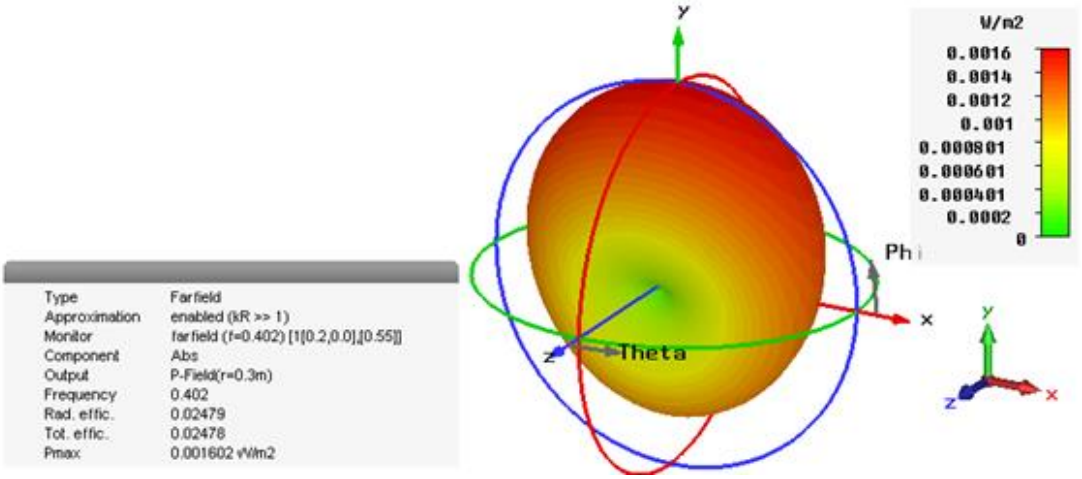

(c) 3D far field pattern of antenna within the humerus.

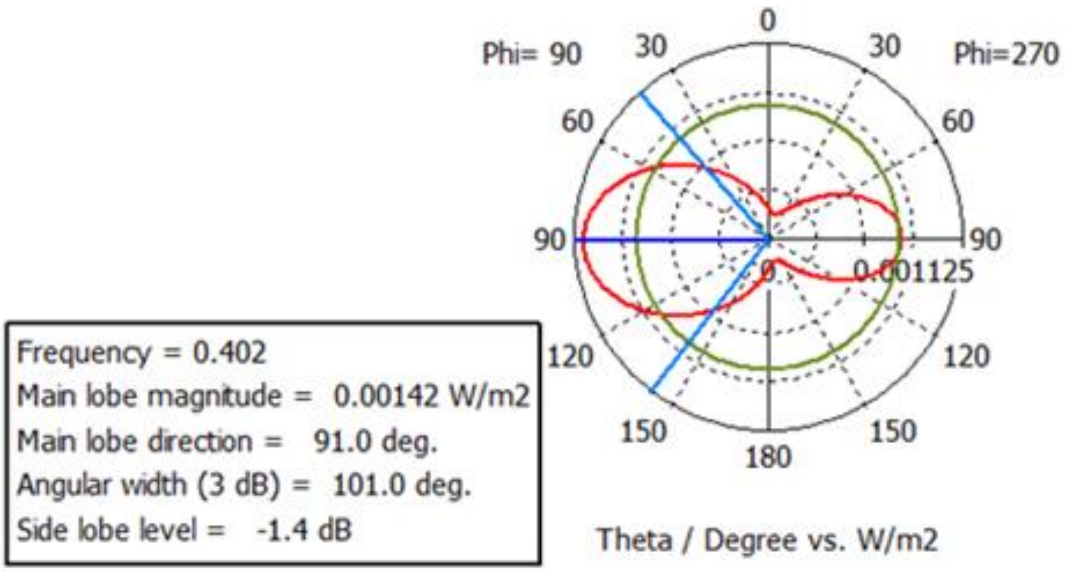

(d) 2D far field pattern of antenna within the humerus.

Figure 38. 3D and 2D far field pattern of the antenna in free space and in humerus

The result of maximum SAR value of the antenna embedded in the human arm tissue is 1.62 W/kg as shown in Figure 39 for the average input power of 20 mW. This value satisfies the IEEE C95 standard.

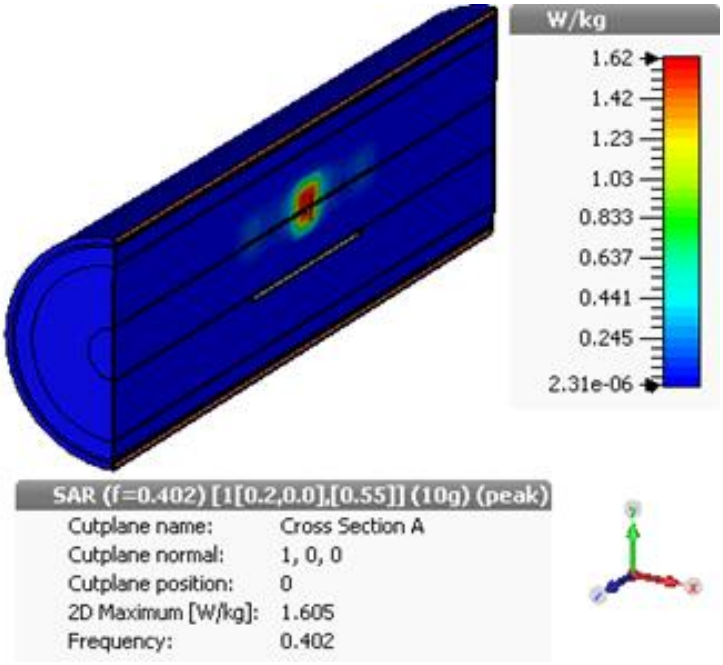

Figure 39. Simulated SAR within the humerus

The simulation of S11, which provides information about the power reflected back from the antenna, shows -38.15 dB in case of normal bone and -15.8 dB, -16.5dB, -15.5 dB for the transverse, 30°, 60° oblique fractures respectively. Figure 40 shows the return loss in cases of normal and the studied types of upper arm fractures.

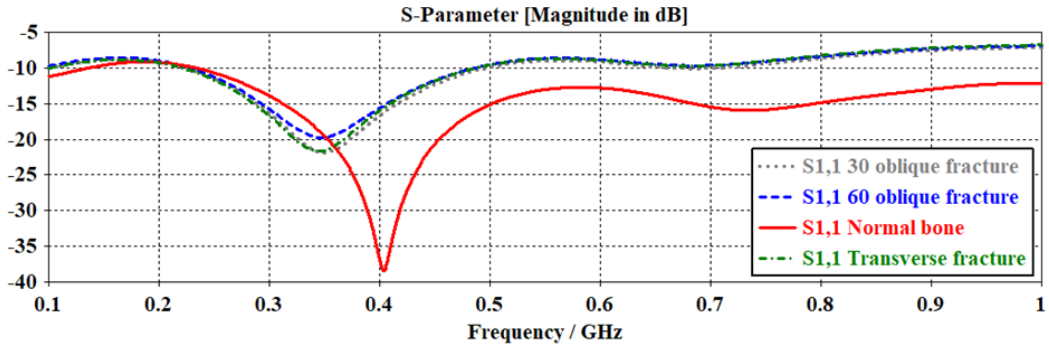

Figure 40. S parameter for normal and fractured humerus.

From the geometry of the 3D pattern shown in Figure 38 (c), 38 (d) we select to test the difference between the transmitted average power densities at two constant ϕ at ±90°. Figure 41 shows a comparison between the transmitted average power density at distance 30 cm in the far field of the antenna for normal and fractured humerus. The observation is recorded at constant values ±90° of ϕ angle at which the maximum transmitted power is obtained. The result of this comparison represents the healing status. Table 18 illustrates the results for the 3 studied types of fracture at the points of maximum transmission.

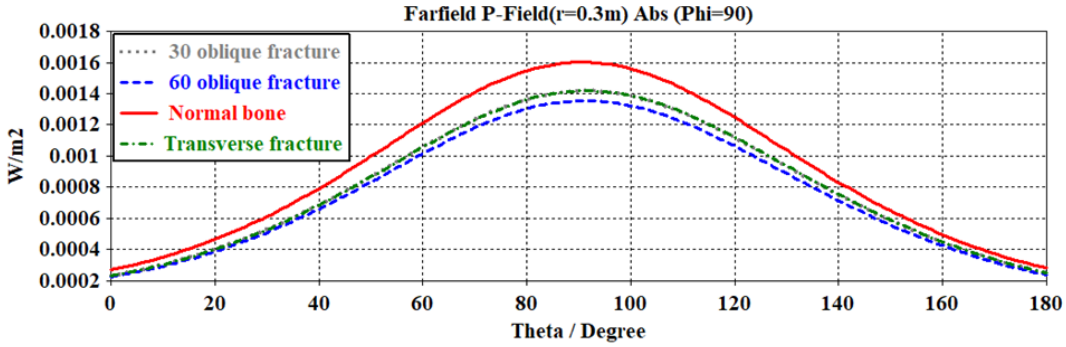

(a)

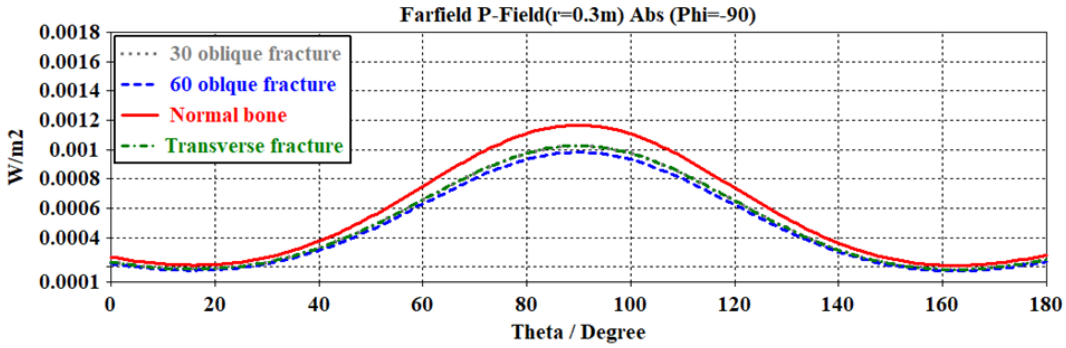

(b)

Figure 41. Variation of transmitted average power density at (a) ϕ =90° and (b) ϕ =-90° for normal humerus, transverse fractured humerus, 30° and 60° oblique fractured humerus.

Table 18. Comparison between transmitted average power density for normal and fractured humerus.

	Humerus status	Normal	Transverse fractured	30° oblique fractured	60° oblique fractured
ϕ = 90°	**Transmitted power density μW/m^2**	1602	1417.6	1417	1354.4
	% Reduction		11.57%	11.54%	15.45%
ϕ = -90°	**Transmitted power density μW/m^2**	1166	1027.5	1026.7	982.4
	% Reduction		11.87%	11.95%	15.75%

Table 18 provides a comparative result of transmitted average power density in cases of normal and fractured humerus. The transmission at $\phi = 90°$ for normal and fractured humerus is higher than that at $\phi = -90°$. This is due to shorter distance that the radiation pass in the lossy tissue medium as this direction excludes the propagation through bone. This shorter path saves 27.2% of the transmitted power density. The percentage reduction of transmission is comparable at the two values of ϕ.

5.3.3 Measurements and validation

In this section, an upper arm of a non-living animal is chosen for carrying out the experimental measurements. The system shown in Figure 42 consists of a vector network analyzer, SMA cables, planar and wire half wave dipole antennas, the animal model, medical splint, fixation plate, and a computer.

(a)

(b)

(c)

(d)

(e)

Figure 42. (a) Humerus model, (b) the fractured bone (c) Antennas and fixation plate, (d) Medical splint, (e) The set

In surgical treatment of such fractures: *first*, the surgeon cuts the skin and muscles to move the bone back into the normal position. *Second*, the metal rod, screws, plates are attached to the bone to hold it. *Finally*, the surgeon closes the incision with stitches or staples, applies a bandage and puts the limb in a cast or splint depending on the location and the type of fracture [48].

In this study we performed the same surgical operation on the selected model by the aid of a specialist. The experiment is based on measuring the reflection coefficient of the implanted antenna in cases of normal and fractured bone.

The measurements are taken in two phases. The first phase represents the model after bone healing completion. We opened the tissue at a length suitable to the dimension of the antenna and the depth is up to the bone. The antenna is implanted between the bone and the muscle tissue. In the opposite side, the tissue is opened and the plate is fixed. The opened tissue is then closed by surgical stitches. The medical splint is added to the model and the reflection coefficient is measured. This step is repeated for both antennas.

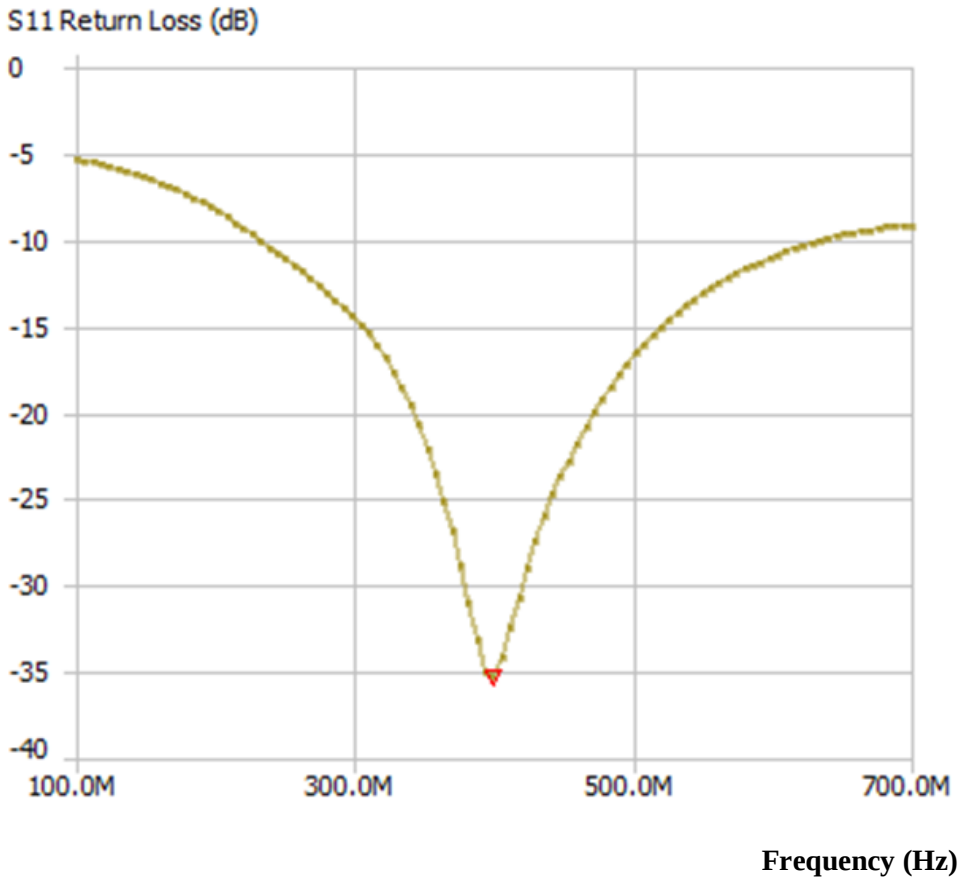

(a) Normal bone, wire antenna.

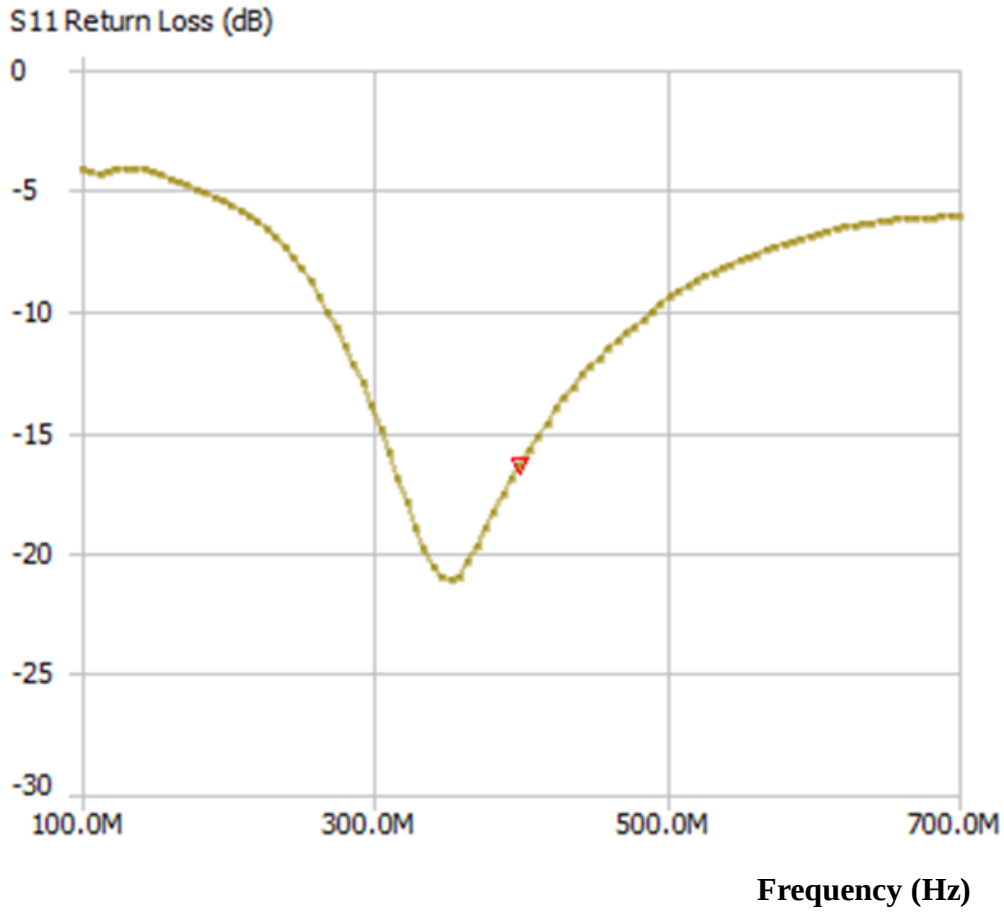

(b) Fractured bone, wire antenna.

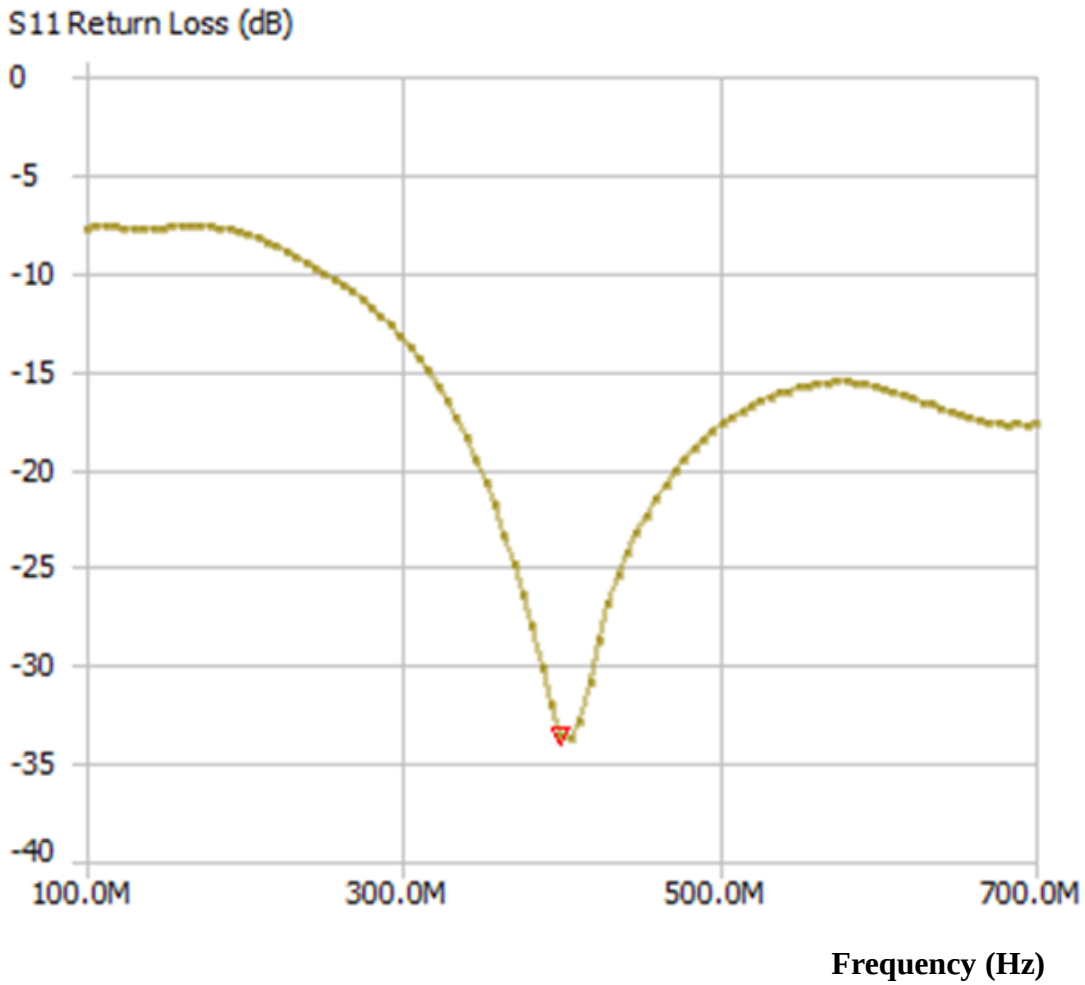

(c) Normal bone, planar antenna.

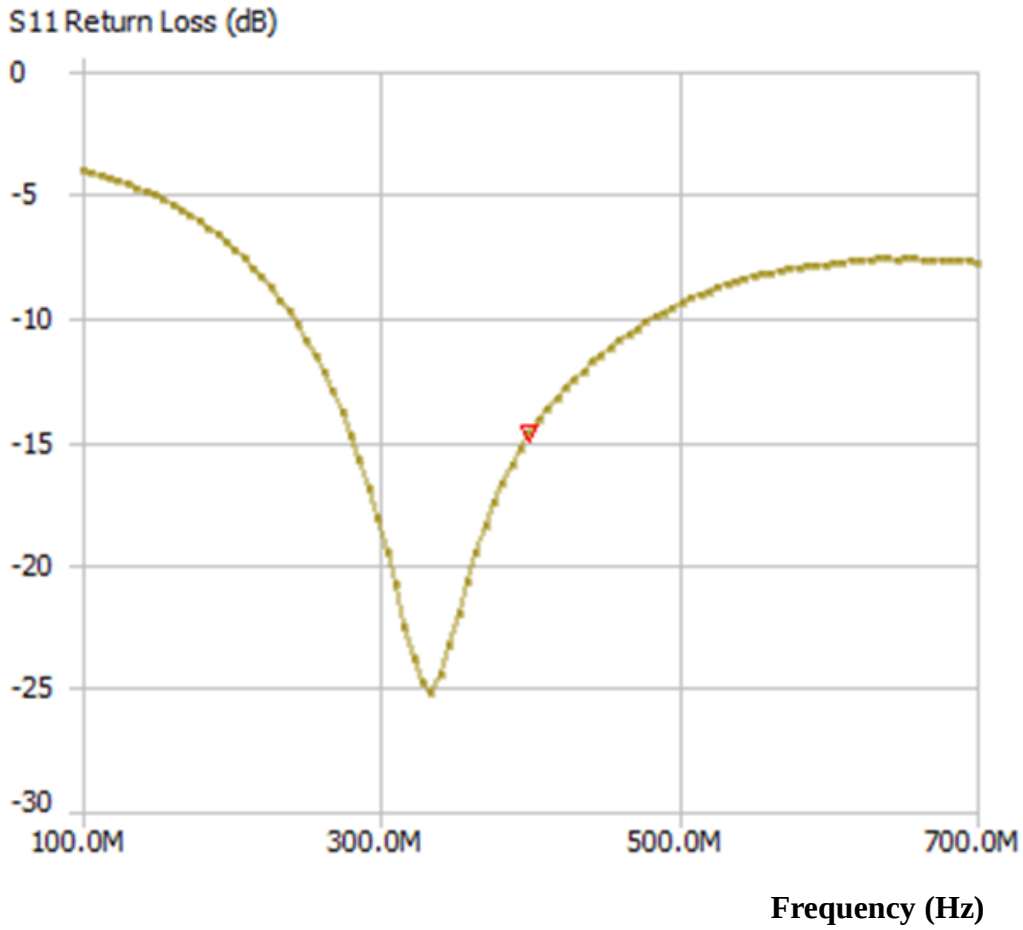

(d) Fractured bone, planar antenna

Figure 43. Measurements of return loss in cases of normal and fractured bone by using wire and planar half wave dipole antennas.

In the second phase, the bone is broken obliquely and the measurements are taken. Figure 43 shows the measurements in cases of normal and fractured bone using both antennas.

The wire antenna was easier in implementation and adjustment of its length to resonate at the operating frequency while it was more difficult than the planar antenna to be fixed within the tissue.

The measurements show good agreement compared to the simulation results. Figure 44 shows the comparison between the results of simulation and measurement for planar and wire antenna.

The experimental measurements show a good matching with the simulation for both topologies of implanted antenna.

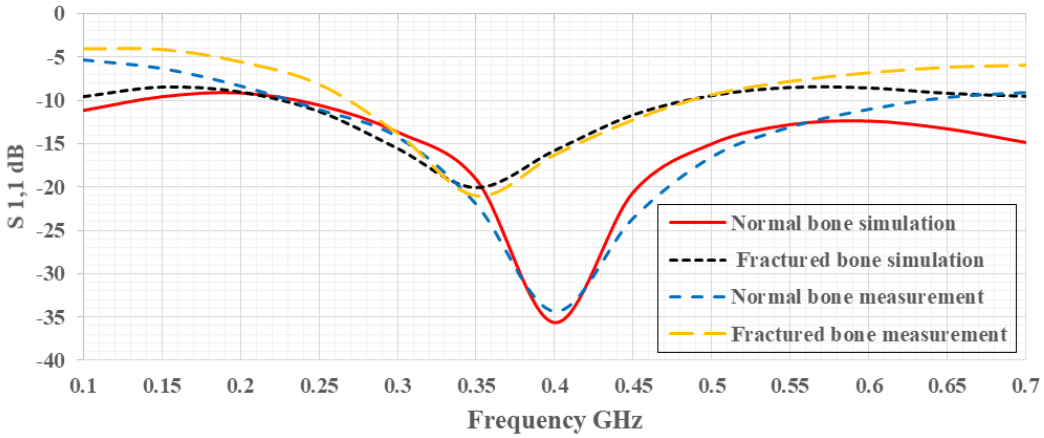

(a) Wire antenna

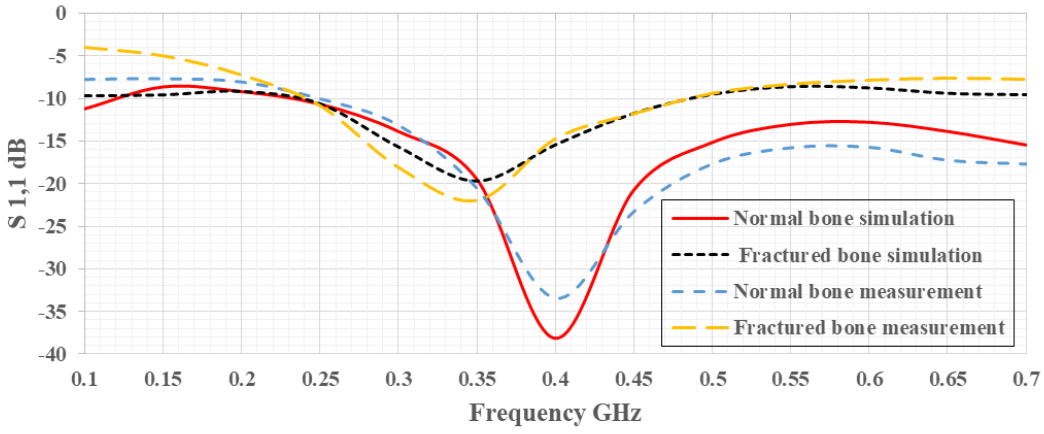

(b) Planar antenna.

Figure 44. Comparison between measurements and simulation results in case of (a) wire antenna, (b) planar antenna.

Chapter 6

CONCLUSION

In this thesis, the remote patient monitoring at which the physiological signals are collected by an implanted device within human body and then transmitted to an external device outside the body for monitoring and controlling is studied. Part of the communication channel between the implanted and the monitoring device is the human tissue. Understanding and characterizing the body channel communication is essential for this type of applications.

First, the characterization and limitation of the in-to-out body channel communication in the MICS and ISM frequency bands is demonstrated. The study presents the range of the EM wave angle of incidence on multilayer human tissue model which produces in-to-out transmission.

A multilayer human tissue model is proposed and analysed for this range of incidence angles. The analysis includes the variation of EM wave reflection coefficient with incident angles, the average power density propagation along the model and the transmission out of it.

A health care monitoring application for the common types of bone fractures healing is proposed. The fracture is represented by an additional layer to the human tissue

model. Different fractures' types are represented by different geometries of the additional layers.

The monitoring method considers the best position of observation of EM wave outside the human body. The angle and position of the observation point are selected such that the AMPD, which is defined by the difference between the average power densities of the normal and fractured bones outside the body, is in its highest value for monitoring the bone fracture healing status.

Planar, and meander half wave dipole antennas are designed and used for the simulation of planar and cylindrical human tissue models. The return loss of the antennas in cases of normal and fractured bone are taken into account.

Considering three θ angles 30°, 60°, 90° at distance 50 cm from the skin, the results of femoral shaft fracture monitoring show that, for both types of bone fractures, the best position of observation at which the AMPD gets the maximum value at $\theta = 30°$, and $\phi = 18°$ to $20°$, or $160°$ to $162°$ for the simulated half wave dipole antennas.

Using the meandered half wave dipole antenna, a 34.15% reduction in the radiator length and 22.9% reduction in the overall length of the antenna are achieved.

The results lead to the importance of oblique angle of transmission and observation of EM wave propagation inside human multilayer tissues for the applications of health care monitoring and in-to-out body channel communication.

To indicate the technique's validity for other human organs that include one bone shaft and muscle, fat, skin tissues like human humerus and tibia fractures, an application for post-surgery monitoring of humerus fractures healing is proposed.

The humerus model in this case includes a fixation plate used in surgery to hold the fractured bone in place during the healing and a medical splint to save the arm in fixed position. Different types of fractures are considered in monitoring. Two different positions of observation are taken into account according to the simulation of far field power pattern of the implanted antenna.

The maximum difference in average power densities is observed at $\phi = 90°$ and $\Theta = 91°$. The results show a reduction of 11.57% to 15.45% of the transmitted average power density when the humerus is broken. This considerable difference for the whole studied fracture types provides information about the bone healing. The return loss shows a remarkable difference between the normal and fractured humerus cases. The standard limits of average specific absorption rate is considered in the antenna design to guarantee its safety for human tissues.

Both femoral shaft and humerus fractures are simulated by CST Microwave studio. The technique is verified experimentally using a lifeless animal model and the results show good agreement with the simulation.

This proposed monitoring method eases the patient's life during the long healing period, especially for elder patients, whom movement is normally difficult, by avoiding repeated visits to laboratories and exposing to X-Ray without any extra surgical operations. Another advantage of monitoring at home is to save the time of

medical staff at hospitals and laboratories for the critical cases that need in sight follow up or treatment.

REFERENCES

[1] Hany Kasaban, M.A.M El-Bendary, Dina .H Salama "A comparative study of Medical imaging techniques" international journal of information science and intelligent systems. 4(2) pp. 37:58, 2015.

[2] Ferlay J., Autier P., Boniol M., Heanue M., Colombet M., and Boyle P. "Estimates of the Cancer Incidence and Mortality in Europe in 2006". Ann Oncol., 18(3):581–92, 2007.

[3] Elice C. Fear, Xu Li, Susan C. Hagness, and Maria A. Stuchly "Confocal Microwave Imaging for Breast Cancer Detection: Localization of Tumors in Three Dimensions". IEEE Transactions on Biomedical Engineering, 49(8):812–822, August 2002.

[4] Robert B. Roemer "Engineering Aspects of Hyperthermia Therapy". Annual Review of Biomedical Engineering, 1:347–376, 1999

[5] Wael Zeinelabedeen and Rasime Uyguroglu" Monitoring of surgically treated upper arm fracture by implanted antenna at 402 MHz." under review.

[6] Yang Li *et al*. "Study on the Electromagnetic field distribution of an Implantable Antenna for Intelligence Health Monitoring System" IEEE Access, VOL. 7, 2019

[7] Francesco Merli, Leandre Bolomey, Jean Z¨urcher, Eric Meurville, and Anja K. Skrivervik, "Versatility and tunability of an implantable antenna for telemedicine,"

5th European Conference on Antennas and Propagation (EuCAP 2011), Rome, Italy, Apr. 11–15, 2011.

[8] Elham Moradi et.al “Miniature implantable and wearable on-body antenna: towards the new era of wireless body centric systems” IEEE Antennas and propagation Magazine, Vol. 56, no. 1, pp272-291, Feb. 2014

[9] Yang Li “Study on the electromagnetic field distribution of an implantable antenna for an intelligence health care monitoring system”. Special section on mission critical sensors and sensor network (MC-SSN) IEEE Access. 2019;7.

[10] Särestöniemi M. “In-body power distribution for abdominal monitoring and implant communication systems”. 16th international symposium on wireless communication systems ISWCS 2019; Oulu, Finland, IEEE 2019.

[11] Li J. “Characterization of in-body radio channels for wireless implants”. IEEE Sens J. March 1, 2017; 17:5.

[12] Fan X. “Detection and diagnosis of paralysis agitans”. IEEE Access. 2018; 6:73023–73029.

[13] Lucisano JY. “Glucose monitoring in individuals with diabetes using a long-term implanted sensor/telemetry system and model”. IEEE Trans Biomed Eng. September 2017

[14] Lakmini P. Malasinghe, Naeem Ramazan, Keshav Dahal “Remote patient monitoring: Acomprehensive study” Journal of ambient intelligence and Humanized computing (2019) 10: pp. 57-76.

[15] Alomainy. “Modelling and characterization of radio propagation from wireless implants at different frequencies”. 9th European Conf. on Wireless Technology. Sept. 2006: 119–122

[16] Roman L-L. “Characterization of path loss and absorption for wireless radio frequency link between an in-body endoscopy capsule and receiver outside the body”. EURASIP J Wirel Commun Netw. 2014; 2014:21.

[17] Kurup D. “In-to-out body antenna-independent path loss model for multilayered tissues and heterogeneous medium”. IEEE Sensors. 2015; 15:408–421. DOI: 10.3390/s 150100408.

[18] Adel Damaj, Hilal M. and Sobhi abou Chahine “Implantable Antenna for Biomedical Applications: An Overview on Alternative Antenna Design Methods and Challenges” 2018 international conference on high performance computing and simulation.pp. 31-37.

[19] Anja K. Skrivervic “Implantable Antennas: The challenge of efficiency” 2013 7th European conference on antenna and propagation EUCAP, pp. 3627-3631.

[20] Anja K. Skrivervik and Francesco Merli “Design Strategies For Implantable Antennas” 2011 Loughbourough Antenna and Propagation conference.

[21] Changrong liu et al. “A Review of implantable antennas for wireless biomedical devices” Forum for Electromagnetic Research Methods and application Technologies (FERMAT) vol.14, 2016.

[22] Syed Ahson and Hyoungsuk Yoo “Scalp-Implantable Antenna systems for Intracranial pressure Monitoring” IEEE Transaction on Antenna and Propagation, Vol. 66, No. 4, April 2016, pp. 2170-2173.

[23] Yihua Zhong, Bolin Qian, Yagoang Zhu “Development of implantable batteryless and wireless bladder pressure monitoring system for lower urinary tract Dysfunction” IEEE journal of Translational Engineering in Health and Medicine. Vol. 8, 2020.

[24] Sourav Sinha et al. “In-body antenna for Monitoring and Controlling Pacemaker” Advances in science, Technology and Engineering Systems Journal, VOL. 5, No. 2, 74-79 (2020).

[25] Florence Kariuki “The Top 13 benefits of remote Patient Monitoring” [Online] Available: https://www.healthrecoverysolutions.com/blog/the-top-13-benefits-of-remote-patient-monitoring

[26] Asswm Sagahyroom “Remote patients monitoring: Challenges” 2017 IEEE 7th annual computing and communication worhshop and conference (CCWC).

[27] Mojtaba Fallahpour and Reza Zoughi “Antenna miniaturization techniques. Arevew of topology and material based methods” Feb. 2018, IEEE Antenna and propagation magazine.

[28] Yei Hwan Jung et al. “A Compact Parylene-Coated Wireless Flexible Antenna For Implantable Electronics” IEEE Antennas and Wireless Propagation Letters, VOL 15, 2016, pp. 1382-1385.

[29] Wael Zeinelabedeen, Rasime Uyguroglu “Characterization of human body channel for oblique incident case of plane wave in the 0.1–10 GHz frequency band for special health care monitoring application”. SIU 2020, The 28th IEEE conference on signal processing and communications applications; Gaziantep, Turkey.

[30] William H. Hayt, Jr. John A. Buck “Engineering Electromagnetics” Sixth edition.

[31] Kurup D. “In-to-out body antenna-independent path loss model for multilayered tissues and heterogeneous medium”. IEEE Sensors. 2015; 15:408–421. DOI: 10.3390/s 150100408.

[32] Chen ZY, Gao YM, Du M. ‘Propagation characteristics of electromagnetic wave on multiple tissue interfaces in wireless deep implant communication”. IET Microw Antennas Propag. 2018; 12(13):2034–2040.

[33] Wael Zeinelabedeen and Rasime Uyguroglu (2021): “A study on health care monitoring of femoral shaft fracture healing by using implanted antenna for

wireless in-to-out body channel communication", Journal of Electromagnetic Waves and Applications, DOI: 10.1080/09205071.2021.1983473.

[34] Sadiku MNO. "Elements of electromagnetics". New York: Oxford University Press; 2007.

[35] Hasgall PA, Di Gennaro F, Baumgartner C, Neufeld E, Lloyd B, Gosselin MC, Payne D, Klingenböck A, Kuster N, "IT'IS Database for thermal and electromagnetic parameters of biological tissues," Version 4.0, May 15, 2018, DOI: 10.13099/VIP21000-04-0. itis.swiss/database.

[36] Yahya Rahamat-Samii and Jaehoon Kim "Implanted antennas in medical wireless communications" Synthesis lectures on antenna #1, Morgan and claypool publishers.

[37] A.Karlsson. "Physical Limitations of Antennas in a Lossy Medium". IEEE Transactions on Antennas and Propagation, 52(8):2027–2033, August 2004.

[38] M.I.Jais et al. "Design analysis of 2.45 MHz meander line antenna (MLA)" 2012 third international conference on intelligent system modelling and simulation.

[39] Sarwak, JF. Rosemont essentials of musculoskeletal care. American Academy of orthopedic surgeons. 2010.

[40] Femur shaft fractures (broken thigh bone). http://orthoinfo.aaos.org/en/diseases–conditions/ femur-shaft-fractures-broken-thighbone/; 2018.

[41] Griffin XL.” Interventions of treating fractures of the distal femur in adults”. 2015. DOI:10.1002/14651858.CD010606.pub2.

[42] Omar AA, Bashayreh QM, Al-Shamali AM. “Investigation of the effect of obliquely incident plane wave on a human head at 900 and 1800 MHZ”. International Journal of RF Microwave and Computer-Aided Engineering “, DOI:10.1002/mmc.

[43] Chen ZY, Gao YM, Du M. “Propagation characteristics of electromagnetic wave on multiple tissue interfaces in wireless deep implant communication”. IET Microw Antennas Propag. 2018;12(13):2034–2040.

[44] Crean TE, Nallamothu SV “Distal humerus fractures” Medline, Jan. 2019.

[45] Launonen AP, Sumrein BO, Reito A et al. “Operative versus non-operative treatment of proximal humeral fractures: A multicentered normalized controlled trial” PLOS Med. Jul. 2019.

[46] Kara N. Bokan, Marlin H. Mickle, Ervin Sejdic “Tissue Variability and Antennas for Power Transfer to wireless implantable Medical Devices” IEEE journal of translational Engineering in Health and Medicine” V5, 2017.

[47] Abdul Qader Khan, Muhammad Riaz, and Anas Bilal “Various Types of Antennas with Respect to their Applications: A Review” International Journal of Multidisciplinary sciences and Engineering. VOL. 7, No. 3, March 2016.

[48] Kristen Nunes “Repairing Major bone Breaks with open Reduction internal Fixation Surgery” Medically reviewed by William Morrison, M.D, January 16, 2019 https://www.healthline.com/health/orif-surgery.